JGP Journal of General Physiology

ARTICLE

ANO1, $Ca_V1.2$, and IP_3R form a localized unit of EC-coupling in mouse pulmonary arterial smooth muscle

Elizabeth J. Akin[1*], Joydeep Aoun[1*], Connor Jimenez[1], Katie Mayne[1], Julius Baeck[1], Michael D. Young[1], Brennan Sullivan[1], Kenton M. Sanders[2], Sean M. Ward[2], Simon Bulley[3], Jonathan H. Jaggar[3], Scott Earley[1], Iain A. Greenwood[4], and Normand Leblanc[1]

Pulmonary arterial (PA) smooth muscle cells (PASMC) generate vascular tone in response to agonists coupled to G_q-protein receptor signaling. Such agonists stimulate oscillating calcium waves, the frequency of which drives the strength of contraction. These Ca^{2+} events are modulated by a variety of ion channels including voltage-gated calcium channels ($Ca_V1.2$), the *Tmem16a* or *Anoctamin-1* (ANO1)-encoded calcium-activated chloride (CaCC) channel, and Ca^{2+} release from the sarcoplasmic reticulum through inositol-trisphosphate receptors (IP_3R). Although these calcium events have been characterized, it is unclear how these calcium oscillations underly a sustained contraction in these muscle cells. We used smooth muscle–specific ablation of ANO1 and pharmacological tools to establish the role of ANO1, $Ca_V1.2$, and IP_3R in the contractile and intracellular Ca^{2+} signaling properties of mouse PA smooth muscle expressing the Ca^{2+} biosensor GCaMP3 or GCaMP6. Pharmacological block or genetic ablation of ANO1 or inhibition of $Ca_V1.2$ or IP_3R, or Ca^{2+} store depletion equally inhibited 5-HT-induced tone and intracellular Ca^{2+} waves. Coimmunoprecipitation experiments showed that an anti-ANO1 antibody was able to pull down both $Ca_V1.2$ and IP_3R. Confocal and superresolution nanomicroscopy showed that ANO1 coassembles with both $Ca_V1.2$ and IP_3R at or near the plasma membrane of PASMC from wild-type mice. We conclude that the stable 5-HT-induced PA contraction results from the integration of stochastic and localized Ca^{2+} events supported by a microenvironment comprising ANO1, $Ca_V1.2$, and IP_3R. In this model, ANO1 and $Ca_V1.2$ would indirectly support cyclical Ca^{2+} release events from IP_3R and propagation of intracellular Ca^{2+} waves.

Introduction

Pulmonary arterial cells constrict in response to agonists coupled to G_q-protein receptor signaling. This process is enhanced in animal models of pulmonary hypertension (PH) and human pulmonary arterial hypertension, where pulmonary arterial smooth muscle cells are more depolarized and display higher intracellular calcium concentrations (Yuan et al., 1998a, 1998b; Lin et al., 2004; Yu et al., 2004; Dai et al., 2005; Hirenallur et al., 2008; Archer et al., 2010). Several ion channels are important for the normal contraction of pulmonary smooth muscle cells and contribute to the development of PH (Mandegar et al., 2002; Mandegar and Yuan, 2002; Yu et al., 2004; Moudgil et al., 2006; Zhang et al., 2007; Archer et al., 2010; Liu et al., 2012; Yamamura et al., 2012; Yang et al., 2012; Xia et al., 2014; Mu et al., 2018). One key protein postulated to play an important excitatory role in agonist-mediated vascular smooth muscle tone is the Ca^{2+}-activated Cl^- channel (CaCC) encoded by the *Tmem16a* or *Anoctamin-1* (ANO1) gene, which has also been implicated to play a major role in PH (Forrest et al., 2012; Sun et al., 2012; Leblanc et al., 2015; Papp et al., 2019). The dogmatic view about the role of ANO1 in electromechanical coupling has been the following (Large and Wang, 1996; Kitamura and Yamazaki, 2001; Leblanc et al., 2005, 2015; Bulley and Jaggar, 2014): (1) stimulation of a G_q protein-coupled receptor (G_qPCR) by a specific agonist leads to the production of inositol-trisphosphate (IP_3) and diacylglycerol resulting from the breakdown of the plasma membrane (PM) phospholipid phosphatidyl-inositol-bisphosphate (PIP_2) catalyzed by the enzyme phospholipase C; (2) IP_3 then binds to one or more of the three IP_3 receptor subtypes expressed in vascular myocytes producing a robust global Ca^{2+} transient originating from the sarcoplasmic reticulum (SR), which in turn activates

[1]Department of Pharmacology and Center of Biomedical Research Excellence (COBRE) for Molecular and Cellular Signal Transduction in the Cardiovascular System, Reno, NV, USA; [2]Department of Physiology and Cell Biology, University of Nevada, Reno School of Medicine, Reno, NV, USA; [3]Department of Physiology, College of Medicine, University of Tennessee Health Science Center, Memphis, TN, USA; [4]Department of Vascular Pharmacology, Molecular and Clinical Science Research Institute, St. George's University of London, London, UK.

*E.J. Akin and J. Aoun contributed equally to this paper. Correspondence to Normand Leblanc: nleblanc@unr.edu.

ANO1; (3) stimulation of ANO1 then causes membrane depolarization due to an equilibrium potential for Cl^- that is ~25–30 mV more positive than the resting potential of the cells (approximately −50 mV; Aickin and Brading, 1982; Chipperfield and Harper, 2000; Sun et al., 2021); and (4) the depolarization triggered by ANO1 stimulates Ca^{2+} entry through voltage-gated Ca^{2+} channels encoded by $Ca_V1.2$, which in turn triggers actin–myosin interaction and contraction by stimulation of myosin light chain kinase.

Although several aspects of the working model described above are correct, the model is too simplistic to explain the complex patterns of Ca^{2+} dynamics observed in smooth muscle cells of intact arteries and veins from the pulmonary circulation. While the membrane depolarization and contraction of pulmonary vascular smooth muscle cells evoked by G_qPCR activation involving agonists such as phenylephrine, serotonin, ATP, angiotensin II, or endothelin-1 are sustained (Yuan, 1997; Forrest et al., 2012; Sun et al., 2012), the underlying Ca^{2+} events are asynchronous, highly localized, and poorly propagating intracellular Ca^{2+} oscillations or waves (Guibert et al., 1996a, 1996b; Hamada et al., 1997; Hyvelin et al., 1998; Smani et al., 2001; Perez and Sanderson, 2005; Perez-Zoghbi and Sanderson, 2007; Henriquez et al., 2018). The disconnect between sustained depolarization and transient, oscillating Ca^{2+} signals suggests that our understanding of pulmonary arterial smooth muscle contraction is incomplete. Since it is well established that the frequency of Ca^{2+} oscillations dictates the strength of contraction, it is important to understand how these Ca^{2+} events are initiated and propagated, as well as the relationship between the ion channels involved.

As mentioned above, ANO1, $Ca_V1.2$, and IP_3 receptors have all been shown to play important roles in pulmonary arterial smooth muscle cell contraction, although the specific contribution and relationship between these channels to create Ca^{2+} oscillations and sustained contractions is not fully understood. Here, we propose that these proteins are localized within microdomains where they form a subcellular signaling complex that supports the Ca^{2+} oscillations and corresponding contraction. This is not without precedence, as recent reports demonstrated the presence of signaling complexes that include ANO1 and IP_3R in dorsal root ganglion neurons (Takayama et al., 2015; Shah et al., 2020). It was demonstrated that ANO1 is not activated by calcium entry through either $Ca_V1.2$ or TRPV1 but rather requires Ca^{2+} release from IP_3R. In cerebral arteries, ANO1 is coupled to TRPC6 to support vasoconstriction (Wang et al., 2016). Here, we sought to investigate whether similar signaling microdomains exist in pulmonary arterial smooth muscle cells.

An additional purpose of this study was to solidify the involvement of ANO1 in agonist-mediated vasoconstriction. Evidence supporting a role for ANO1 in the vasoconstriction mediated by agonists has largely stemmed from studies reporting a significant attenuation by both classical and newer generations of CaCC/ANO1 blockers. Several of the newer generation of inhibitors (De La Fuente et al., 2008; Namkung et al., 2011; Huang et al., 2012; Oh et al., 2013) have been suggested to produce non-specific effects as reported by Boedtkjer et al. (2015), who showed that $T16A_{Inh}$-A01, $CaCC_{Inh}$-A01, and MONNA all produced a vasorelaxation of precontracted arteries in the "absence" of a transmembrane Cl^- gradient. $T16A_{Inh}$-A01 also directly blocked macroscopic L-type Ca^{2+} current recorded in A7r5 smooth muscle cells and high KCl-induced contractions in intact arteries, while MONNA hyperpolarized non-stimulated resting vascular smooth muscle through an unknown mechanism (Boedtkjer et al., 2015). Thus, there is a question of whether the participation of ANO1 in electromechanical coupling and the development of arterial smooth muscle tone has been overestimated.

In this study, we used conditional smooth muscle–specific and inducible ANO1 knockout mice to define the role of ANO1 in determining the contractile and intracellular Ca^{2+} signaling properties of endothelium-denuded mouse pulmonary arterial smooth muscle exposed to the agonist serotonin (5-HT) and test the effectiveness and specificity of $CaCC_{Inh}$-A01. Our data show that suppressing ANO1, $Ca_V1.2$, or Ca^{2+} release from IP_3R-sensitive Ca^{2+} stores in the SR similarly reduced the contraction to 5-HT by ~50–60%. Asynchronous Ca^{2+} oscillations evoked by 5-HT were potently inhibited by similar approaches. Since our data demonstrate that ANO1, $Ca_V1.2$, and IP_3R all functionally contribute to smooth muscle contraction, we investigated whether they are localized to microdomains. A specific ANO1 antibody was able to pulldown both $Ca_V1.2$ and IP_3R in total protein lysates from pulmonary arteries, and advanced microscopy techniques revealed that $Ca_V1.2$ and IP_3R colocalize with ANO1, especially near the PM. These experiments suggest that the stable 5-HT-induced pulmonary arterial contraction results from the integration of stochastic and localized Ca^{2+} events supported by a molecular architecture comprising ANO1, $Ca_V1.2$, and IP_3R, which coordinates fundamental signaling optimized for excitation–contraction (EC) coupling.

Materials and methods

Animals and dissection of intact pulmonary arteries

All procedures pertaining to housing conditions and animal handling were approved by the University of Nevada Institutional Animal Care and Use Committee (protocol #20-06-1016-1) in accordance with the Update of the Guide for the Care and Use of Laboratory Animals by the National Research Council of the National Academies (8th edition, 2011). Five mouse strains were used in this study: (1) C57/BL6; (2) B6;129S-Gt(ROSA)26Sor$^{tm38(CAG-GCaMP3)Hze}$/J/SmMHC-CreERT2 (SMC-GCaMP3); (3) B6J.Cg-*Gt(ROSA)26Sor*$^{tm95.1(CAG-GCaMP6f)Hze}$/MwarJ/SmMHC-CreERT2 (SMC-GCaMP6f); (4) 129S-Gt(ROSA)26Sor$^{tm38(CAG-GCaMP3)Hze}$/J/SmMHC-CreERT2/ANO1fl/fl-ΔExons 5–6 (SMC-ANO1-kO-$^{\Delta Ex5-6}$-GCaMP3); and (5) B6;129S-Gt(ROSA)26Sor$^{tm38(CAG-GCaMP3)Hze}$/J/SmMHC-CreERT2/ANO1fl/fl-ΔExon 12 (SMC-ANO-kO-$^{\Delta Ex12}$/GCaMP3). For the four transgenic mouse models used, the induction of Cre recombinase expression was elicited by three consecutive daily IP injections with tamoxifen (TMX; MilliporeSigma; 80 mg/kg dissolved in safflower seed oil), and experiments were carried out between 50 and 60 d following the last TMX injection.

Upon removal, the heart and lungs were immediately immersed in cold (4°C) well-oxygenated Krebs solution of the

following composition (in mM): 120 NaCl, 25 $NaHCO_3$, 4.2 KCl, 1.2 KH_2PO_4, 1.2 $MgSO_4$, 1.8 $CaCl_2$, and 5.5 glucose (pH stabilized to 7.4 when bubbled with 95% O_2–5% CO_2). The main pulmonary artery was carefully dissected away from the heart and lungs and cleaned of any fat and connective tissue. For all contraction and Ca^{2+} imaging experiments, the endothelium was removed by passing a continuous stream of air bubbles through the lumen of the blood vessel via a syringe. This procedure abolished the endothelium-dependent relaxation caused by 1 µM acetylcholine in pulmonary arteries precontracted with 1 µM serotonin.

Contraction experiments in intact pulmonary arterial rings

Pulmonary arterial (PA) rings of ∼250 µm in length and <100 µm in diameter were mounted on a Four-Channel WPI Myobath II System to record isometric force. Each PA ring was mounted on a fixed stainless-steel pin at one end and to a stainless-steel triangular hook at the other end, itself hooked to a force transducer attached to a holder equipped with fine micropositioning to stretch the artery to a desired basal tension. Once mounted, the ring was immersed in a heated water-jacketed chamber filled with 30 ml of Krebs solution (composition identical to that described in the previous section) bubbled with 95% O_2–5% CO_2 (pH 7.4) and maintained at 37°C. The analog signal from the force transducer was recorded and measured using an A/D data acquisition system (by means of one of two WPI TBM4 amplifiers, and one MP100 or MP100A-CE A/D system from BIOPAC Systems, Inc.) and Acknowledge (v.3.9; BIOPAC Systems) software running on a Windows 10-based PC. Each PA ring was equilibrated in normal Krebs solution for at least 30 min. During this period, basal tension was set to 1 g. After equilibration, the ring was submitted to two consecutive 10-min incubation challenges with high K^+–Krebs solution to elicit smooth muscle contraction by membrane depolarization and assess the viability of the preparation; the two challenges were interspersed by a 20-min wash in normal Krebs. Preparations were rejected when peak contraction was more than two standard deviations away from the mean. The high K^+–Krebs solution was prepared by replacing 80 mM NaCl with 80 mM KCl, yielding a final K^+ concentration = 85.4 mM. Following the second high K^+–Krebs solution challenge, the solution was switched to normal Krebs solution for 10 min before the experiment was begun. Experiments were initiated by incubating each PA ring for 10 min with vehicle (0.1% DMSO) or one of four pharmacological agents: 1 µM nifedipine (MilliporeSigma), 10 µM cyclopiazonic acid (CPA; MilliporeSigma), 1 µM xestospongin C (Abcam), or 10 µM $CaCC_{Inh}$-A01 (MilliporeSigma). This was followed by a protocol designed to generate a cumulative dose–response curve to the agonist 5-HT, which was directly added to the bath as a concentrated stock solution (final concentrations were 0.01, 0.03, 0.1, 0.3, 1, 10, and 30 µM). Incubation with each 5-HT concentration usually lasted ∼5–10 min. In separate experiments, we tested the effects of agents on the high K^+ Krebs-mediated contraction. Once a plateau was reached during the second high K^+–Krebs solution challenge, the preparation was then exposed to vehicle (0.1% DMSO), 1 µM nifedipine, or to four concentrations of $CaCC_{Inh}$-A01 added in sequence (1, 3, 10, and 30 µM), all directly added to the chamber as concentrated stock solutions dissolved in DMSO (0.1%). For each preparation, peak contraction measured in a specific condition (5-HT ± drug, or high K^+–Krebs solution + drug) was normalized to the peak contraction evoked by the second high K^+–Krebs solution challenge. Finally, for experiments designed to determine the total amount of Ca^{2+} stored in the SR, after the second challenge with high K^+–Krebs solution, the solution was either changed to normal Krebs for 20 min (control) or for 10 min followed by a 10-min incubation with normal Krebs solution containing either 1 µM nifedipine or 10 µM $CaCC_{Inh}$-A01. For each of these conditions, the solution was then switched to Ca^{2+}-free Krebs solution containing 100 µM EGTA and 10 µM CPA to block the SR Ca^{2+}-ATPase, with or without 1 µM nifedipine or 10 µM $CaCC_{Inh}$-A01. The latter solution elicited a transient contraction produced by the transient release of Ca^{2+} from the SR. The transient contraction was integrated and normalized to the amplitude of the second challenge with a high K^+–Krebs solution; this ratio was used as an indirect index of the total amount of Ca^{2+} stored in the SR.

Isolation of mouse pulmonary artery smooth muscle cells

Single smooth muscle cells were freshly isolated from the main trunk and secondary branches of mouse pulmonary arteries using a technique adapted from the acute method described by Pritchard et al. (2014) for rat PASMCs. In brief, dissected pulmonary arteries were first incubated for 1 h at 4°C in a dissociation medium (DM; description below) containing the enzyme papain (1.5 mg/ml; Sigma-Aldrich). The composition of the DM was the following (in mM): 110 NaCl, 5 KCl, 0.5 KH_2PO_4, 0.5 NaH_2PO_4, 10 $NaHCO_3$, 0.16 $CaCl_2$ (free $[Ca^{2+}]$ = 7.6 µM), 2 $MgCl_2$, 0.5 EDTA, 10 D-glucose, 10 taurine, and 10 Hepes-NaOH (pH 7.4). The partially digested tissue was then incubated for 6 min at 37°C with DM containing papain (1.5 mg/ml; MilliporeSigma) and the reducing agent dithiothreitol or DTT (1 mg/ml; MilliporeSigma). This was followed by a final enzymatic step during which the pulmonary arteries were incubated for 5–10 min in DM containing collagenase type IA (1.0–1.5 mg/ml; MilliporeSigma) and protease type XIV (1 mg/ml; MilliporeSigma). The remaining tissue was subsequently rinsed twice in enzyme-free DM. Cells were then dispersed by gentle trituration of the remaining digested tissue for ∼2 min using a small-bore Pasteur pipette. The remaining supernatant containing PASMCs was stored for 2–6 h at 4°C until use for imaging or electrophysiological experiments.

Whole-cell patch clamp electrophysiology

Ca^{2+}-activated Cl^- currents (I_{ClCa}) were recorded from freshly isolated mouse pulmonary artery smooth muscle cells (PASMC) using the conventional whole-cell configuration of the patch clamp technique using an Axopatch 200B amplifier (Molecular Devices), Digidata 1320A acquisition system (Molecular Devices) and pCLAMP 9 software (Molecular Devices). To reduce contamination of I_{ClCa} from other types of currents in our recordings, CsCl and tetraethylammonium chloride (TEA) were added to the pipette solution and TEA was added to the K^+-free external solution. The external solution used in all patch-clamp experiments had the following composition (in mM): 126 NaCl, 10

Hepes (pH adjusted to 7.35 with NaOH), 8.4 TEA, 20 glucose, 1.2 $MgCl_2$, and 1.8 $CaCl_2$. The intracellular pipette was set to 1 µM free [Ca^{2+}] by the addition of 10 mM BAPTA and 8.27 mM $CaCl_2$, which was calculated using the calcium Chelator program MaxChelator (v. 2.51; Patton, 2010). The internal pipette solution contained the following (in mM): 20 TEA, 106 CsCl, 10 Hepes (pH adjusted to 7.2 with CsOH), 10 BAPTA, 8.27 $CaCl_2$, 5 ATP.Mg, 0.55 $MgCl_2$ (1 mM free [Mg^{2+}]), and 0.2 guanosine-5′-triphosphate. Series resistance compensation was performed in all experiments. Cells were continuously superfused with the external solution at a flow rate of ∼1 ml/min. All electrophysiological experiments were performed at room temperature.

I_{ClCa} was evoked immediately upon rupture of the cell membrane and its voltage-dependent properties were monitored every 10 s by stepping from a holding potential (HP) of −50 to +90 mV for 1 s, followed by repolarization to −80 mV for 1 s. Current–voltage (I–V) relationships were constructed after ∼2 min of cell dialysis by stepping in 10 mV increments from HP to test potentials between −100 and +140 mV for 1 s, each step followed by a 1 s repolarizing step to −80 mV. For I–V relationships, I_{ClCa} was expressed as current density (pA/pF) by dividing the current amplitude measured at the end of each voltage clamp step by the cell membrane capacitance (C_m in pF), which was calculated by integrating the average of five consecutive capacitive current (I_C) transients elicited by steps to −60 mV from HP = −50 mV and using the following equation: $C_m = \int I_C.dt/\Delta V$, where dt is time (in ms) and ΔV corresponds to the 10 mV hyperpolarizing steps.

Ca^{2+} imaging in intact pulmonary arteries

A freshly dissected endothelium-denuded pulmonary artery from a mouse expressing either GCaMP3 or GCaMP6f conditionally in smooth muscle cells was cut open and pinned down with its lumen facing up on a 35-mm Petri dish layered with Sylgard. The Petri dish was then moved to the stage of an upright Olympus BX50WI epifluorescence microscope where constant flow superfusion (∼1 ml/min) with a normal physiological salt solution (PSS; see composition below) was initiated using a Gilson Minipulse 3 peristaltic pump with solutions maintained at 37°C by means of a temperature-controlled water-jacketed glass coil circulated by a Cole Palmer Polystat Controller pump. The composition of the PSS was as follows (in mM): 135 NaCl, 10 $NaHCO_3$, 4.2 KCl, 1.2 KH_2PO_4, 1.2 $MgCl_2$, 1.8 $CaCl_2$, 5.5 glucose, and 10 Hepes-NaOH (pH 7.35). The preparation was allowed to equilibrate for a minimum of 30 min before fluorescence imaging was started. Imaging of GCaMP3/GCaMP6f-expressing smooth muscle cells was performed from the luminal side of the artery by means of one of three water immersion objectives (LUMPlan FNL 60×/0.9 NA, 40×/0.75 NA, or 20×/0.5 NA). GCaMP3 or GCaMP6f was excited at a wavelength of 488 nm by a Lumencor IIluminator Spectra X solid-state light source transmitted to the microscope via an optical fiber. 500–1,000 images (512 × 512 pixels) were acquired at 31 frames/s by an Andor iXon EMCCD camera (Andor Technology) controlled by Andor SOLIS software (Andor Technology) running under a Windows 7 PC platform. Movie stack TIFF files were analyzed using public domain ImageJ (Schneider et al., 2012). Each stack was first submitted to background subtraction (30–50 roll ball radius) followed by two rounds of smoothing. Three spatio-temporal (ST) maps were then generated per movie by reslicing three areas of the image using the line function of ImageJ at a width of 3 pixels and using a 90° rotation and avoiding interpolation. The three lines used to create ST maps across the entire image were drawn perpendicularly to the long axis of the smooth muscle cells and in a few pilot studies along the cell axis. The latter strategy was used to assess potential intercellular propagation of Ca^{2+} transients. The fluorescence intensity of all cells was measured from ST maps using the line function of ImageJ at a width of 3 pixels. The fluorescence intensity profile was then plotted as a function of time and the data were transferred to Excel and OriginPro (v. 2021b; OriginLab) for data analysis. GCaMP3 or GCaMP6f fluorescence (F) was reported as F/F_0, where F_0 is baseline fluorescence. When photobleaching was apparent, traces were corrected by subtracting a straight line from the baseline and then adding a value of one to each data point. Time-dependent fluorescence intensity profiles were analyzed using the Gadgets Quick Peaks module of OriginPro. This feature allowed for automated detection and analysis of Ca^{2+} transients. The module was generally set for detection of peaks by height at the 20% default value, which was sometimes raised when Ca^{2+} transients were small and noisy. Peak height, integrated area under the curve, and full-width duration at half-maximum (FWHM) were calculated by OriginPro. The frequency in Hertz was calculated in Excel by dividing the number of Ca^{2+} transients detected by the total duration of the movie in seconds (16.13 or 32.26 s).

Confocal microscopy

Pulmonary artery smooth muscle cells were freshly isolated as described above and plated onto no. 1.5H microscope cover glass (Deckgläser). Cells were fixed with 3.2% formaldehyde/0.1% glutaraldehyde in a DM for 10 min at room temperature, rinsed three times with PBS, then blocked and permeabilized using a solution containing 0.1% Triton-X 100, 1% BSA, and 20% SEA block (Thermo Fisher Scientific) in PBS for 1 h at RT. Cells were incubated overnight at 4°C with primary antibodies: rabbit antibody to ANO1 (PA2290, 1:50; Boster Biological), mouse antibody to $Ca_V1.2$ (N263/31, 1:100; NeuroMab), or mouse antibody to IP_3R (sc-377518, 1:100; Santa Cruz). Samples were washed with PBS three times and incubated with Alexa Fluor 647-conjugated goat anti-rabbit or Alexa Fluor 488-conjugated goat anti-mouse secondary antibodies (1:1,000; Invitrogen) at room temperature for 1 h, then washed three to five times with PBS. Slides were imaged using an Olympus FluoView FV 1000 laser scanning confocal microscope with an Olympus 100× UPlanApo100XO 1.40 NA oil immersion objective or a Leica Stellaris 8 confocal microscope equipped with a 100× objective.

Superresolution nanomicroscopy

Sample preparation was performed as described above for immunolabeling with the addition of extra 15-min wash steps with PBS. Samples were mounted on glass depression slides with the wells filled with a Glox-MEA Imaging Buffer as outlined in Dixon

et al. (2017) and the edges of the coverslip were sealed with Twinsil (Picodent). Images were acquired on a GSDIM imaging system (Leica) built around an inverted microscope (DMI6000B; Leica) using a 160× HCX Plan-Apochromat (1.47 NA) oil-immersion lens and an EMCCD camera (iXon3 897; Andor Technology). Lateral chromatic aberrations and astigmatism corrections are integrated into the Leica GSDIM systems in parallel to the objective, tube lens, and c-mount. Optimal image results were obtained through the interplay of these corrections. Images were acquired in both TIRF and epifluorescence modes. The incidence angle for the TIRF mode was 150 nm. 25,000–60,000 frames were acquired for each color. Dual color images were acquired sequentially, with the Alexa Fluor 647-conjugated signal (ANO1) acquired first followed by the Alexa Fluor 488-conjugated signal (either IP_3R or $Ca_V1.2$).

Image reconstruction was performed using the ImageJ plugin ThunderSTORM (Ovesný et al., 2014) using the default settings. Colocalization and nearest-neighbor analyses were determined using the ThunderSTORM coordinate-based colocalization (CBC) algorithm. Clusters were analyzed using SR-Tesseler (Levet et al., 2015). The program segments the single-molecule localizations and identifies regions of higher density. Clusters were defined as regions with localizations 2.5 times greater than surrounding areas.

RNA extraction and qRT-PCR

Total RNA was extracted using Trizol (Life Technologies) according to the manufacturer's instructions. cDNA was prepared using a high-capacity cDNA Reverse Transcription Kit (Applied Biosystems). Quantitative analysis of mRNA expression was performed on a QuantStudio3 system (Thermo Fisher Scientific). 20 µl reactions (1 µl cDNA, 200 nM [ANO1] or 500 nM [β-actin] of each forward and reverse primer, and SYBR Green PCR master mix, Applied Biosystems) were run in triplicate. The normalized mRNA expression was calculated according to the ($2^{\Delta\Delta Ct}$) method.

Coimmunoprecipitation (co-IP)

For each experiment, ice-cold radioimmunoprecipitation buffer (RIPA) with a protease inhibitor cocktail was used to harvest lysate from pulmonary arteries pooled from five to six C57/BL6 mice. co-IP was performed using Pierce Protein A/G Agarose. Briefly, the pulmonary arterial lysate was incubated with rabbit anti-ANO1 polyclonal antibody (ab53212; Abcam) at 4°C overnight. 20 µl Protein A/G Agarose resin was added and incubated for another 2 h at room temperature to capture the antibody–antigen complex. Antibody bound resin was then centrifuged and washed with RIPA buffer and bound proteins were eluted using denaturing buffer. The boiled eluate was run on an SDS-polyacrylamide gel and protein samples were analyzed by Western blotting.

Protein analysis and Western blotting

Pulmonary artery from five to six C57/BL6 mice were homogenized and lysed in RIPA lysis buffer containing a cocktail of protease inhibitors. Proteins were separated in 4–12% NuPAGE (Thermo Fisher Scientific) and transferred into nitrocellulose membranes (0.45 µm; cat. no. 162-0215; Bio-Rad). The membranes were blocked with LI-COR Odyssey blocking buffer (part no. 92740000) in PBS (1:1) for 1 h at room temperature and incubated overnight at 4°C with the following primary antibodies (all diluted at 1:250 in LI-COR Odyssey blocking buffer in PBS [1:1] with 0.01% Tween-20): rabbit polyclonal ANO1 (ab53212; Abcam), rabbit monoclonal IP_3R (D53A5; Cell Signaling Technology), mouse monoclonal polyclonal $Ca_V1.2$ (MAB13170; MilliporeSigma), and goat polyclonal actin (sc-1616; Santa Cruz Biotechnology). The membranes were incubated with Alexa Fluor 680 or 800 conjugated goat anti-rabbit IgG or donkey anti-goat (diluted 1:25,000 in LI-COR Odyssey blocking buffer in PBS [1:1] with 0.01% Tween-20) for 1 h at room temperature. Signals were detected using Odyssey Infrared Imaging System (LI-COR) near infrared wavelengths using the 700 and 800 nm channels. All experiments were performed in triplicate.

Statistical analysis

All pooled data are expressed as means with error bars representing the SEM. Raw data were imported into Excel and the means exported to OriginPro 2021b software (OriginLab Corp.) for plotting and testing of statistical significance between groups. Statistical significance between means was determined using paired or unpaired Student's *t* test when two groups were compared, or one-way or two-way ANOVA for multiple group comparisons, and the Tukey's post hoc test to determine which groups are statistically significant from each other. $P < 0.05$ was considered to be statistically significant. All graphs, images, and ionic current traces were uploaded to CorelDRAW 2021 for Mac for final processing of the figures.

Online supplemental material

Video 1 depicts the lack of spontaneous activity in an intact pulmonary artery from a conditional SMC-GCaMP3 mouse exposed to a normal external solution. Video 2 shows that a 5-min exposure to 1 µM 5-HT triggered asynchronous Ca^{2+} oscillations in the same pulmonary artery from a conditional SMC-GCaMP3 mouse as shown in Video 1. Video 3 is a Surface Plot video illustrating the initiation and propagation of Ca^{2+} waves in a single PASMC from an intact pulmonary artery from a conditional SMC-GCaMP3 mouse. Video 4 shows that a 10-min exposure to 10 µM $CaCC_{Inh}$-A01 in the presence of 5-HT had a profound inhibitory effect on Ca^{2+} oscillations in the same pulmonary artery from a conditional SMC-GCaMP3 mouse as shown in Videos 1 and 2.

Results

ANO1 promotes agonist-mediated contraction of mouse pulmonary arteries

We first evaluated the contribution of ANO1, voltage-gated Ca^{2+} channels (VGCC), and Ca^{2+} release from the SR in the contraction elicited by the agonist 5-HT of endothelium-denuded wild-type C57/BL6 mouse pulmonary arteries using wire myography. Fig. 1 A shows two typical experiments in which a cumulative dose-response curve to 5-HT was generated in the absence (Fig. 1 A; Control) or presence of the ANO1 inhibitor $CaCC_{Inh}$-A01 (Fig. 1

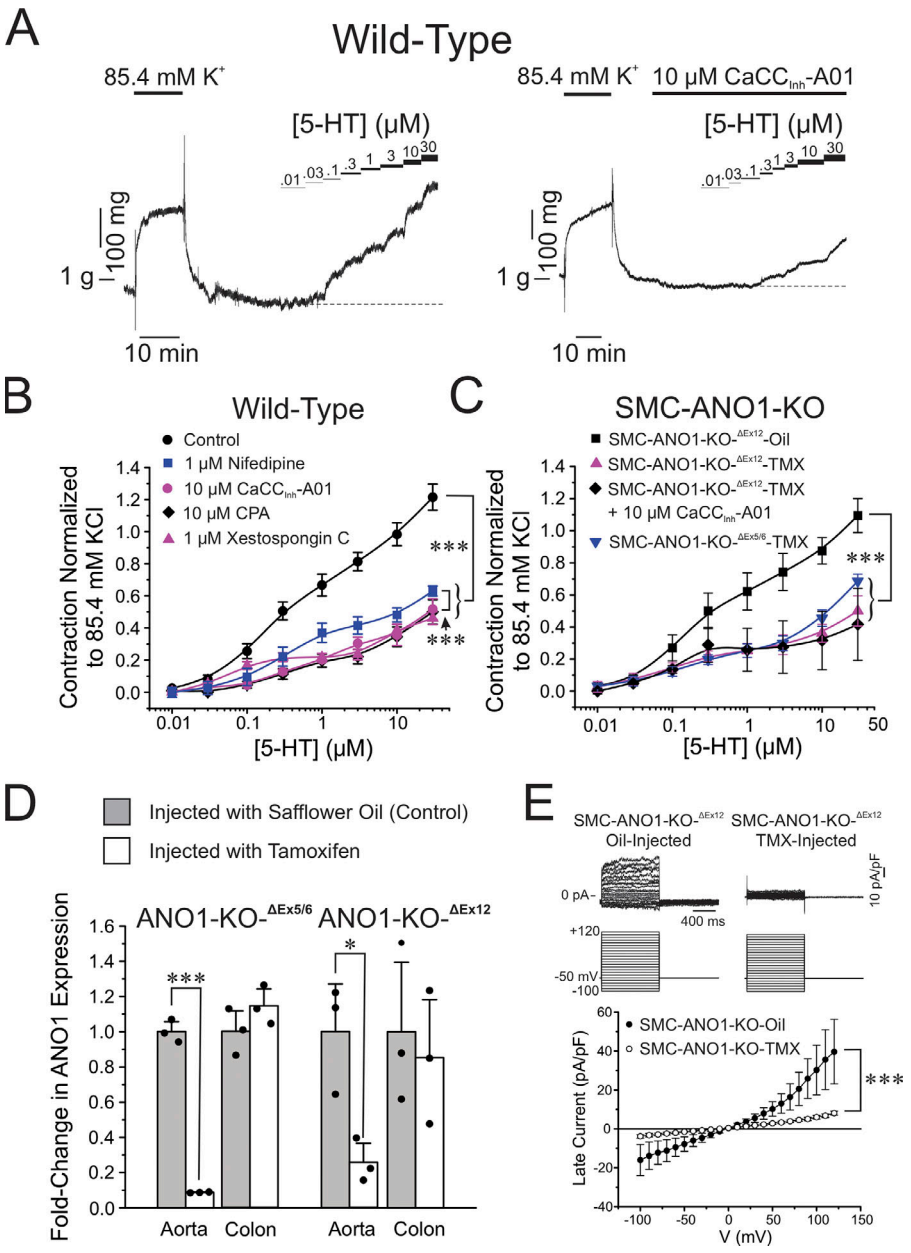

Figure 1. **Pharmacological block or genetic knockdown of ANO1 produces a similar inhibition of the contraction of mouse pulmonary artery to 5-HT as blocking VGCC or emptying Ca^{2+} stores from the SR. (A)** Typical isometric force recordings in response to high K^+ Krebs (85.4 mM) and increasing cumulative concentrations of 5-HT ranging from 0.01 to 30 μM as indicated by the bars above the traces, in the absence (left) or presence (right) of the ANO1 inhibitor $CaCC_{Inh}$-A01, also indicated by a horizontal bar above the trace. **(B)** Mean cumulative dose–response curves to 5-HT in mouse pulmonary arteries from wild-type C57/BL6 mice in the absence (black circles, Control; n = 14), or presence (blue squares; n = 5) of 1 μM nifedipine to block VGCC, 10 μM CPA to deplete SR Ca^{2+} stores (black diamonds; n = 4), 10 μM $CaCC_{Inh}$-A01 (magenta circles; n = 6) to block ANO1, or 1 μM xestospongin C to block IP_3R (magenta triangles; n = 6). Each data point is a mean ± SEM of net contractile force normalized to the second high K^+–Krebs solution-induced contraction (see examples in A and description in Materials and methods). **(C)** Mean cumulative dose–response curves to 5-HT in mouse pulmonary arteries from two conditional smooth muscle-specific and inducible ANO1 KO mice (SMC-ANO1-KO), one with floxed ANO1 flanking exons 5 and 6 (SMC-ANO1-KO-$^{\Delta Ex5/6}$), and the other with floxed ANO1 flanking exon 12 (SMC-ANO1-KO-$^{\Delta Ex12}$). The cumulative dose–response relationship to 5-HT in SMC-ANO1-KO-$^{\Delta Ex12}$ injected with safflower oil served as a control (black squares; SMC-ANO1-KO-$^{\Delta Ex12}$-Oil; n = 4) and displayed remarkable similarity to the control curve obtained with wild-type mice (B). SMC-ANO1-KO-$^{\Delta Ex12}$ injected with tamoxifen (TMX) led to a significant reduction in contraction amplitude (upper magenta triangles; SMC-ANO1-KO-$^{\Delta Ex12}$-TMX; n = 5), which was unaffected by exposure to 10 μM $CaCC_{Inh}$-A01 (black diamonds; n = 3). The magnitude of the contraction to 5-HT for tamoxifen-injected SMC-ANO1-KO-$^{\Delta Ex5/6}$ mice was also reduced to a similar extent to that exerted by exon 12 deletion (inverted blue triangles; n = 5). **(D)** Reverse-transcription qPCR demonstrating ANO1 knockdown in aortic smooth muscle but not colonic tissue from both SMC-ANO1-KO mice used in this study (ANO1-KO-$^{\Delta Ex5/6}$ and ANO1-KO-$^{\Delta Ex12}$). Measurements were performed between 50 and 60 d after injection with safflower seed oil (light gray bars) or tamoxifen (open bars). ANO1 expression was normalized to β-actin. Each overlaid data point represents one animal; * and ***, significantly different from control with $P < 0.05$ and $P < 0.001$, respectively. **(E)** Ca^{2+}-activated Cl^- currents were abolished in PASMCs from SMC-ANO1-KO mice. Top: Typical families of Ca^{2+}-activated Cl^- currents (I_{ClCa}) recorded in PASMCs from SMC-ANO1-KO-$^{\Delta Ex12}$ injected with vehicle (oil-injected; traces on the left) or tamoxifen (TMX-injected; traces on the right). Currents evoked with a pipette solution set to 1 μM Ca^{2+} were recorded in response to the voltage-clamp protocol shown below the traces. Bottom: Mean current–voltage relationships for I_{ClCa} measured at the end of voltage-clamp steps ranging from −100 to +120 mV from a holding potential of −50 mV in PASMCs from SMC-ANO1-KO-$^{\Delta Ex12}$ mice injected with vehicle (SMC-ANO1-KO-Oil; filled circles) or tamoxifen (SMC-ANO1-KO-TMX; open circles). Each data point is a mean ± SEM SMC-ANO1-KO-Oil: N = 2, n = 5; SMC ANO1-KO-TMX: N = 4, n = 8; with N and n representing the number of animals and cells, respectively. For all panels, *** and * indicate a significant difference between means with $P < 0.001$ and $P < 0.05$, respectively.

A, right). For all experiments, only a single concentration–response relationship to 5-HT was generated in each preparation since pilot experiments revealed a significant attenuation of the response to a second 5-HT challenge, presumably due to receptor desensitization. The threshold concentration of 5-HT eliciting a measurable contraction in control condition was 30 nM (Fig. 1 A). $CaCC_{Inh}$-A01 (10 μM) significantly decreased peak contraction at all 5-HT concentrations tested and shifted the threshold concentration evoking a contraction to ∼300 nM (Fig. 1 A, right). The concentration of $CaCC_{Inh}$-A01 was chosen on the basis that it was previously shown to block ∼90% of expressed mouse ANO1 current in a voltage-independent manner (IC_{50} = 1.7 μM; Bradley et al., 2014), and caused no significant effect on the contraction to high K^+ solution (85.4 mM; Fig. 2, A

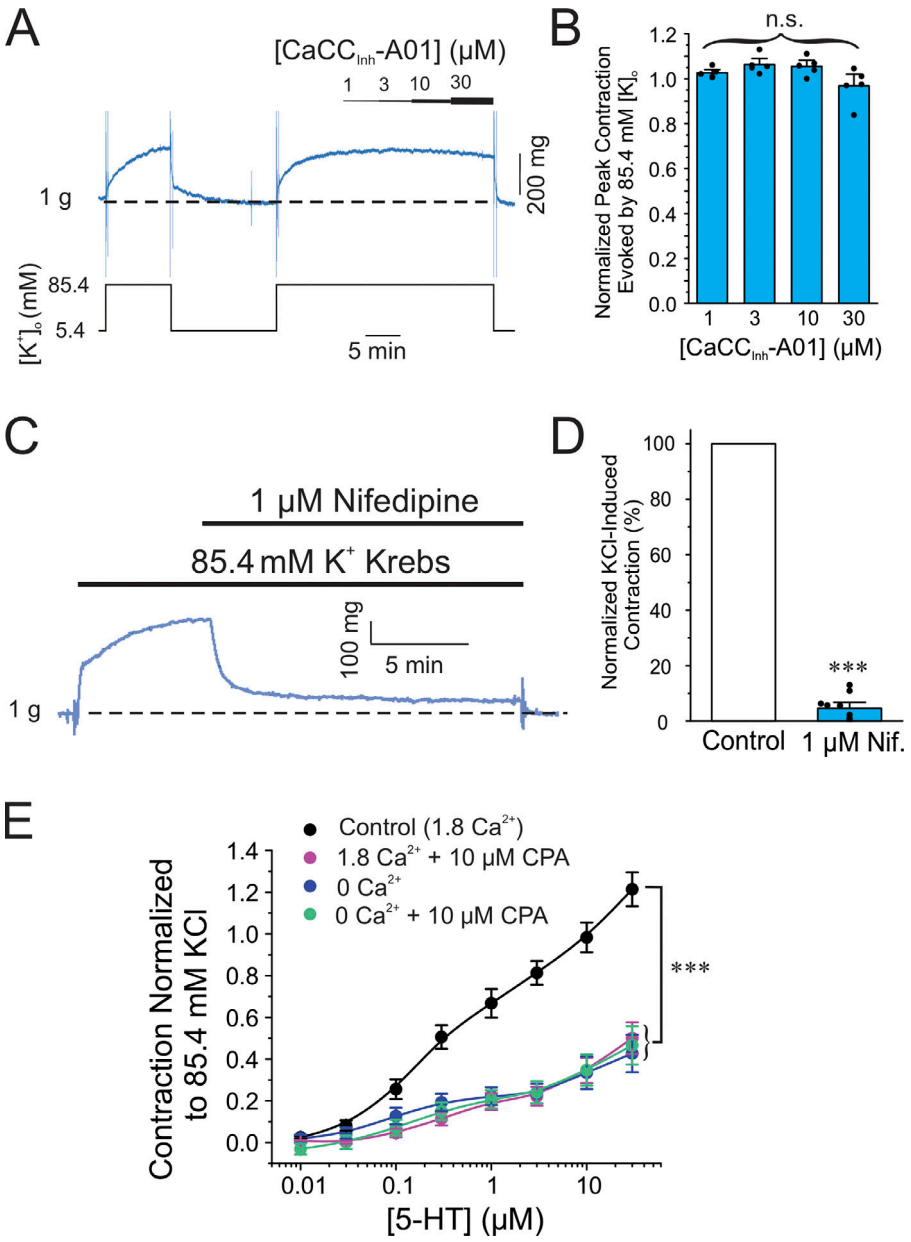

Figure 2. **The ANO1 blocker CaCC$_{Inh}$-A01 produced no effect on the high K$^+$-mediated contraction of the mouse pulmonary artery.** **(A)** Typical contractile force experiment showing that increasing the concentration of CaCC$_{Inh}$-A01 from 1 to 30 μM (progressively thickening black bar shown over the trace) produced no noticeable effect on the contraction (blue trace) elicited by 85.4 mM K$^+$–Krebs solution (K$^+$ concentration changes are indicated with the black line below the contraction trace). **(B)** Mean bar graph summarizing the effects of different concentrations of CaCC$_{Inh}$-A01 on the contraction elicited by high K$^+$–Krebs solution as in A. Contractile force at each concentration of CaCC$_{Inh}$-A01 was normalized to the net contraction elicited by high K$^+$–Krebs solution obtained during the prior wash with this solution as shown on the left side of A. Each bar represents the mean ± SEM and data points overlaid on each bar represents individual animals (N = 5). **(C)** Typical contraction experiment showing the potent block produced by the Ca$_V$1.2 blocker nifedipine (Nif.; 1 μM; top black bar) on the contraction (blue trace) elicited by 85.4 mM K$^+$–Krebs solution (bottom black bar). **(D)** Mean bar graph summarizing the effects of nifedipine on the contraction mediated by high K$^+$–Krebs solution as in A. The mean net contractile force measured in the presence of nifedipine was normalized to that measured in the absence of the drug just prior to its addition (blue bar). The bar with nifedipine is a mean ± SEM. Overlaid data points represent different animals (N = 10). **(E)** Mean cumulative dose–response curves to 5-HT in mouse pulmonary arteries from wild-type C57/BL6 mice in the presence of normal extracellular Ca^{2+} concentration with (magenta circles; 1.8 Ca^{2+} + 10 μM CPA; N = 4) or without (black circles, Control [1.8 Ca^{2+}]; N = 14) 10 μM CPA to deplete SR Ca^{2+} stores, or in Ca^{2+}-free with (green circles; 0 Ca^{2+} + 10 μM CPA; N = 6) or without (blue circles; 0 Ca^{2+}; N = 18) CPA. Each data point is mean ± SEM of net contractile force normalized to the second high K$^+$–Krebs solution-induced contraction (see examples in A and description in Materials and methods). The control (1.8 Ca^{2+}) and 1.8 Ca^{2+} + CPA curves were reproduced from Fig. 1 B. For all panels, *** indicates a significant difference between means with $P < 0.001$; n.s.: not significant.

and B). The latter observation is important as it indicates that the compound exerted no direct effect on the contractile machinery, or VGCC, which contrasts with the potent inhibitory effect of the Ca^{2+} channel blocker nifedipine on this contraction (1 μM; Fig. 2, C and D). In the control condition, the concentration–response curve to 5-HT was biphasic (Fig. 1 B), an observation possibly attributable to the presence of 5-HT$_{1B/1D}$ and 5-HT$_{2A}$ receptor subtypes as identified in pulmonary arteries from several mammalian species including human, mouse, and rat (Uma et al., 1987; Cortijo et al., 1997; Shaw et al., 2000; Liu and Folz, 2004; Perez and Sanderson, 2005; Rodat-Despoix et al., 2009). The biphasic nature of the concentration–response relationship to 5-HT was still apparent following the block of ANO1 by CaCC$_{Inh}$-A01 (Fig. 1 B). Blocking VGCC with nifedipine, emptying SR Ca^{2+} stores with CPA (Seidler et al., 1989), or blocking the IP$_3$R with xestospongin C (Gafni et al., 1997) produced very similar effects to those caused by the ANO1 inhibitor (Fig. 1 B), even though the curve obtained with nifedipine was slightly elevated relative to those of CaCC$_{Inh}$-A01, CPA, and xestospongin C, likely attributable to an incomplete block of VGCC with 1 μM nifedipine (Fig. 2, C and D). Remarkably, the concentration–response curve to 5-HT in the presence of CPA was also similar to preparations exposed to Ca^{2+}-free solution or Ca^{2+}-free in the presence of CPA (Fig. 2 E). These results suggest that activation of store-operated Ca^{2+} entry (SOCE) by CPA-induced store depletion in the presence of

Table 1. **Effects of various treatments on parameters calculated from dose–response relationships to 5-HT**

	EC_{50} (nM)	Maximum 5-HT contraction amplitude (normalized to KCl)	Slope factor *p*	*N*	Mean R^2
Wild-type					
Control	209 ± 34	0.784 ± 0.073	1.57 ± 0.25	14	0.993 ± 0.004
Nifedipine	355 ± 117	**0.451 ± 0.065***	1.46 ± 0.33	5	0.997 ± 0.003
$CaCC_{Inh}$-A01	673 ± 274	**0.332 ± 0.059****	1.33 ± 0.25	6	0.957 ± 0.019
CPA	309 ± 40	**0.238 ± 0.045*****	1.70 ± 0.44	4	0.996 ± 0.002
Xestospongin C	70 ± 10	**0.294 ± 0.068*****	1.93 ± 0.22	6	0.989 ± 0.003
0 Ca^{2+}	211 ± 43	**0.290 ± 0.060*****	1.46 ± 0.30	11	0.986 ± 0.005
0 Ca^{2+} + CPA	142 ± 19	**0.306 ± 0.031*****	1.12 ± 0.11	6	0.985 ± 0.011

Individual dose–response curves to 5-HT were least-square fitted to a logistic function of the following formalism: $Y = A1 + [(A2 - A1)/(1 + ([5\text{-HT}]/EC_{50})^p)]$, where Y is the contraction amplitude registered in the presence of 5-HT normalized to the high KCl-induced contraction, A1 and A2 are the minimum and maximum contraction amplitudes, respectively, [5-HT] is the concentration of 5-HT, EC_{50} is the concentration of 5-HT producing a contraction that is 50% of maximum, and *p* is the slope factor. Because of the biphasic nature of the dose–response curves to 5-HT (see Fig. 1 and text for explanation), only the initial portion of each curve, thus ranging from 0.01 to 1 or 3 µM 5-HT, was analyzed to calculate the parameters shown in the table. All values are means ± SEM pooled from 4 to 14 animals (*N*). One-way ANOVA tests revealed significant differences in the contraction amplitude between treatments and the control group (bolded numbers) with *P < 0.05, **P < 0.01, and ***P < 0.001. All other comparisons were not significant.

normal extracellular Ca^{2+} did not produce a significant contractile effect in our conditions. We least-square fitted individual dose-response relationships to 5-HT to a monophasic logistic function for all conditions. Only the initial component of the biphasic response was analyzed by restricting the fitting range from 0.01 to 1–3 µM 5-HT. This is because a maximum effect for the second component at higher concentrations of 5-HT was not clearly discernable. Table 1 summarizes mean data obtained for the estimated EC_{50}, maximum contraction amplitude, and slope factor *p*, and provides a mean R^2 for each condition. While there were no significant differences between each group and the control group for the EC_{50} and slope factor *p*, all treatments produced a significant inhibition of the maximum contraction amplitude, in accord with our two-way ANOVA analyses of these curves.

We repeated similar experiments in PA from two conditional smooth muscle-specific and inducible ANO1 KO mice, both driven by TMX-sensitive Cre expression under the control of the smooth muscle myosin heavy chain promoter located on the Y chromosome (*Myl1*). ANO1 knockdown induced by TMX is mediated by the deletion of *loxP* sequences flanking exons 5 and 6, or exon 12. Both animal models also conditionally express the Ca^{2+} biosensor protein GCaMP3 under the control of the same *Cre-lox* system (SMC-ANO1-kO-$^{\Delta Ex5\text{-}6}$-GCaMP3 and SMC-ANO1-kO-$^{\Delta Ex12}$-GCaMP3). The cumulative concentration-response curve to 5-HT of PA from SMC-ANO1-kO-$^{\Delta Ex12}$-GCaMP3 animals injected with vehicle (oil; Fig. 1 C) was nearly superimposable to that obtained from wild-type mice (Fig. 1 B), displaying a similar threshold around 30 nM, a biphasic relationship and a similar peak contraction at the highest concentration of 5-HT. ANO1 knockdown resulted in a significantly reduced concentration–response curve to 5-HT that mimicked that obtained in PA from wild-type mice exposed to $CaCC_{Inh}$-A01, nifedipine, CPA, or xestospongin C (Fig. 1 B). A very similar profile was registered in PA from SMC-ANO1-kO-$^{\Delta Ex5,6}$-GCaMP3 mice (Fig. 1 C). We also fitted these relationships using the same approach as that described in Table 1. As for the effects of various inhibitory conditions on PA from wild-type mice, a decrease in maximal contraction amplitude was the only parameter that was significantly affected and reduced by ANO1 knockdown (Table 2). Notably and importantly, the EC_{50} and maximum contraction amplitude estimated for wild-type and oil-injected SMC-ANO1-kO-$^{\Delta Ex12}$-GCaMP3 mice were remarkably similar with an EC_{50} of ∼210 nM and maximum contraction amplitude of ∼0.8 (normalized to KCl).

Real-time quantitative PCR experiments revealed a marked reduction in the expression of ANO1 mRNA in the aorta of both animal models (>75%), but not in the colon (Fig. 1 D). This is consistent with ANO1 in the colon being expressed almost exclusively in c-Kit$^+$ interstitial cells of Cajal where they play a major role in driving pacemaker activity and initiating slow waves, but not in smooth muscle cells in this tissue (Huang et al., 2009; Hwang et al., 2009; Zhu et al., 2009; Berg et al., 2012; Sanders et al., 2012). Consistent with a reduced expression of ANO1 protein, Ca^{2+}-activated Cl^- currents in PASMCs from SMC-ANO1-kO-$^{\Delta Ex12}$-GCaMP3 mice treated with TMX were abolished (Fig. 1 E). Finally, $CaCC_{Inh}$-A01 exerted no additional effects on the PA contraction of SMC-ANO1-kO-$^{\Delta Ex12}$-GCaMP3 (Fig. 1 C). These results indicate that a high level of knockdown of ANO1 protein was achieved in PASMCs in both transgenic mouse models injected with TMX. They also suggest that the inhibitory effects of $CaCC_{Inh}$-A01 in PA from wild-type mice specifically targeted ANO1.

ANO1 is key for maintaining 5-HT-mediated Ca^{2+} signaling

We used fluorescence imaging to explore the mechanisms involved in the effects of 5-HT on changes in intracellular Ca^{2+} concentration in intact endothelium-denuded PA from transgenic mice conditionally expressing the Ca^{2+} reporter GCaMP3, specifically in smooth muscle cells. Spontaneous Ca^{2+} transients were detected in some preparations in the absence of 5-HT, but these were extremely rare events and were therefore not

Table 2. **Parametric comparisons of dose–response relationships to 5-HT generated in wild-type and conditional smooth muscle–specific ANO1 KO mice**

	EC_{50} (nM)	Maximum 5-HT contraction amplitude (normalized to KCl)	Slope factor *p*	*N*	*Mean* R^2
Wild-type					
Control	209 ± 34	0.784 ± 0.073	1.57 ± 0.25	14	0.993 ± 0.004
ANO1-KO Δ exon 12					
Oil-injected control	210 ± 36	0.771 ± 0.105	1.14 ± 0.17	4	0.993 ± 0.002
TMX-injected	125 ± 24	**0.250 ± 0.034**[a,b]	1.54 ± 0.31	5	0.981 ± 0.008
ANO1-KO Δ exons 5/6					
TMX-injected	195 ± 72	**0.316 ± 0.056**[a,c]	0.96 ± 0.15	5	0.924 ± 0.062

Individual dose–response curves to 5-HT were least-square fitted to a logistic function of the following formalism: $Y = A1 + [(A2 - A1)/(1 + ([5\text{-HT}]/EC_{50})^p)]$, where Y is the contraction amplitude registered in the presence of 5-HT normalized to the high KCl-induced contraction, A1 and A2 are the minimum and maximum contraction amplitudes, respectively, [5-HT] is the concentration of 5-HT, EC_{50} is the concentration of 5-HT producing a contraction that is 50% of maximum, and *p* is the slope factor. Because of the biphasic nature of the dose–response curves to 5-HT (see Fig. 1 and text for explanation), only the initial portion of each curve, thus ranging from 0.01 to 3 µM 5-HT, was analyzed to calculate the parameters shown in the table. All values are means ± SEM pooled from 4 to 14 animals (*N*). One-way ANOVA tests revealed significant differences in the maximum contraction amplitude between animal groups as shown (bolded numbers).
[a]P < 0.01 versus wild-type control.
[b]P < 0.01 versus ANO1-KO Δ exon 12.
[c]P < 0.05 versus ANO1-KO Δ exon 12.

analyzed (Fig. 3 A and Video 1). Exposure to 1 µM 5-HT elicited asynchronous Ca^{2+} oscillations at a frequency of ~1.5 Hz (Fig. 3 B and Video 2). Ca^{2+} transients analyzed by creating ST maps along the longitudinal axis of the smooth muscle cells revealed that Ca^{2+} transients propagated as waves within the cell but did not spread from cell to cell (Fig. 4 A). Lack of or poor cell-to-cell propagation of these Ca^{2+} transients was also evident when analyzed orthogonally from the long axis of the cells (Fig. 4 A). These results are in agreement with the concept that each cell generates its own Ca^{2+} oscillations producing sustained force integrated over time by the frequency and amplitude of Ca^{2+} transients (Perez-Zoghbi and Sanderson, 2007). Although not analyzed in detail, Ca^{2+} transients were generally initiated from a few regions or "hot spots" in the cell. An example is shown in Fig. 4 B, where Ca^{2+} waves were randomly triggered from either end of the cell and propagated unidirectionally, or an area near the nucleus that propagated bidirectionally toward the cell ends. Video 3 highlights these properties. 5-HT-induced Ca^{2+} transients were nearly abolished by $CaCC_{Inh}$-A01 in PA from SMC-GCaMP3 mice (Fig. 3 C and Video 4) and potently inhibited by genetic knockdown of ANO1 (SMC-ANO1-kO-$^{\Delta Ex12}$-GCaMP3; Fig. 5). We systematically analyzed several parameters of Ca^{2+} transients recorded in different conditions and preparations. Fig. 6 shows that blocking ANO1 with $CaCC_{Inh}$-A01 or blocking VGCC with nifedipine in PA from SMC-GCaMP3 mice (Control; light blue bars) led to a quantitatively similar reduction in frequency (Fig. 6 A), peak Ca^{2+} transient amplitude (Fig. 6 B), and integrated area under the curve (Fig. 6 C); the duration of Ca^{2+} transients measured at half-amplitude was significantly reduced by $CaCC_{Inh}$-A01, but not by nifedipine (Fig. 6 D). Depleting Ca^{2+} stores with CPA abolished Ca^{2+} oscillations (Fig. 6 A). Importantly, genetic deletion of ANO1 in SMC-ANO1-kO-$^{\Delta Ex12}$-GCaMP3 mice (light gray bars) produced a reduction in the frequency and duration of Ca^{2+} transients (Fig. 6, A and D) relative to control, but did not significantly alter peak amplitude and integrated area under the curve (Fig. 6, B and C). Taken together, these results suggest that the Ca^{2+} oscillations evoked by 5-HT are supported by the coordinated stimulation of ANO1, Ca^{2+} entry through VGCC ($Ca_V1.2$), and Ca^{2+} release from the SR, most likely from IP_3R.

ANO1 and $Ca_V1.2$ are critical for refilling SR Ca^{2+} stores

The results presented so far suggest that Ca^{2+} release from IP_3R is the predominant Ca^{2+} source generating Ca^{2+} oscillations and contractility in response to 5-HT, and the feedback loop between ANO1 and $Ca_V1.2$ may be key for reloading SR Ca^{2+} stores. We tested this hypothesis by examining the effects of blocking ANO1 or $Ca_V1.2$ on the amount of Ca^{2+} stored in the SR. This was indirectly assessed by measuring the transient contraction produced by blocking the SR Ca^{2+}-ATPase with 10 µM CPA in the absence of external Ca^{2+}. Fig. 7 A shows an isometric force recording illustrating the impact of switching the external solution from normal Krebs containing 1.8 mM Ca^{2+} to the Ca^{2+}-free/CPA solution. As highlighted by the red area under the trace, the latter solution produced a robust transient contraction that was evoked by Ca^{2+} mobilization from the SR. In contrast, a 10-min exposure to 1 µM nifedipine or 10 µM $CaCC_{Inh}$-A01 to block $Ca_V1.2$ (Fig. 7 B) or ANO1 (Fig. 7 C), respectively, markedly inhibited this contraction. We quantified the effects of the two inhibitors by integrating the area under the curve for the transient contraction (highlighted in red in A–C) and normalizing it to the amplitude of contraction caused by the high K^+–Krebs solution that preceded the 0 Ca^{2+}/CPA protocol (contraction to high KCl shown on the left side of A–C). Fig. 7 D indicates that $CaCC_{Inh}$-A01 and nifedipine produced a strong inhibition of the contraction elicited by 0 Ca^{2+}/CPA; there was no significant difference between the two drug treatments. These experiments support the concept that the main function of ANO1 and $Ca_V1.2$ is to refill Ca^{2+} stores in the SR to support cyclical Ca^{2+} release through IP_3R.

ANO1, $Ca_V1.2$, and cortical IP_3R form functional coupling sites at SR/PM junctional microdomains for efficient Ca^{2+} signaling in mouse PASMCs

The combination of the functional observations described above with the very low number of detectable sites in each cell found to initiate Ca^{2+} waves led us to hypothesize that ANO1 and $Ca_V1.2$ in the PM and IP_3R in closely juxtaposed SR contact areas may be

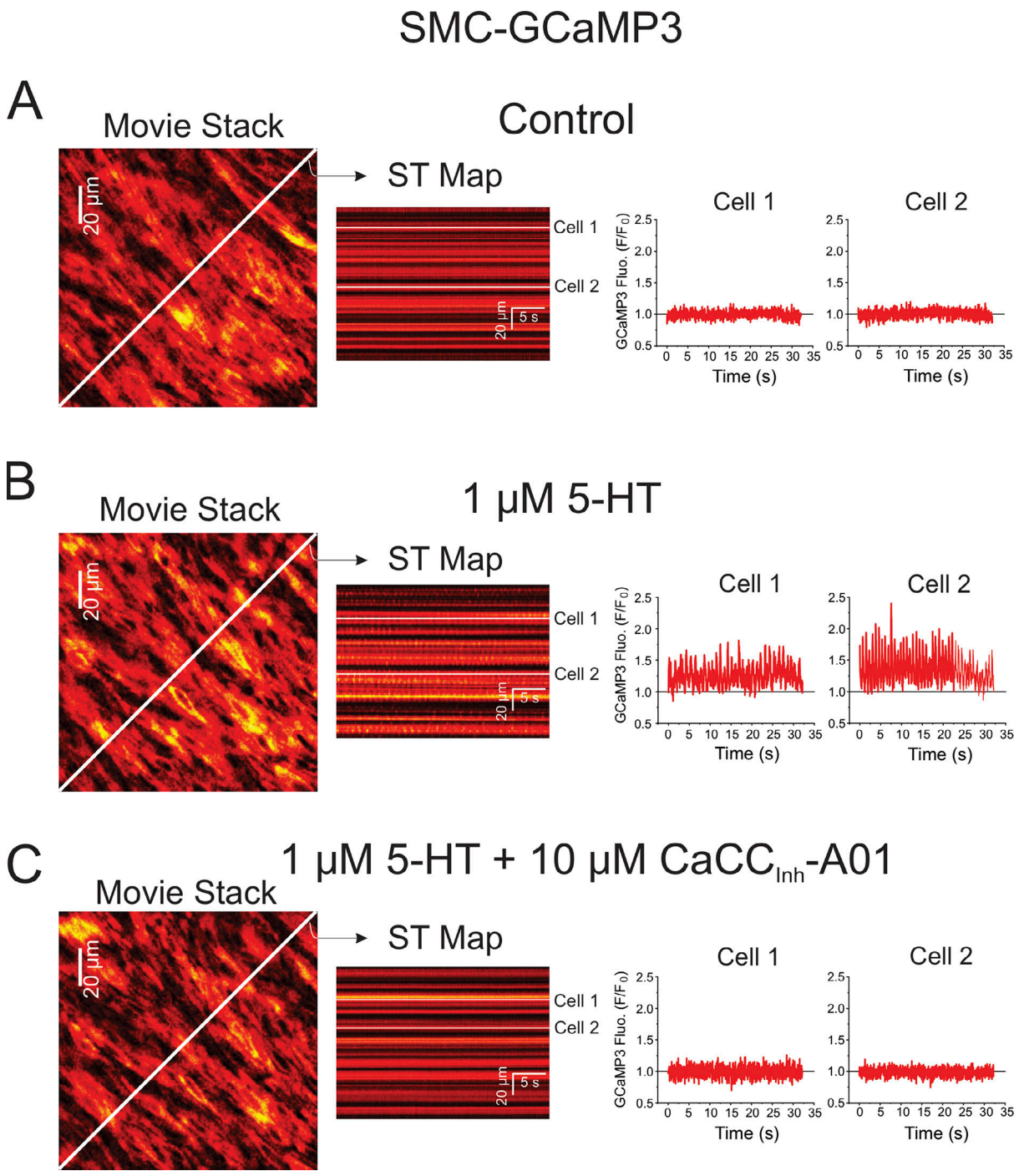

Figure 3. **Ca^{2+} oscillations triggered by 5-HT in individual smooth muscle cells from an intact mouse endothelium-denuded PA are potently inhibited by the inhibition of ANO1.** All data were collected from the same PA from a conditional smooth muscle–specific and inducible GCaMP3 mouse injected with tamoxifen to induce Cre expression. **(A)** Ca^{2+} imaging was performed in the absence of an agonist (Control). The left panel shows one image from a video from which a ST map (middle colored image) was created in the area spanned by the diagonal white line. Fluorescence intensity was measured under the three white lines on the ST map (corresponding to two different cells) and plotted as a function of time as shown on the right. There was no detectable activity in these two cells as well as across the entire field of view of the movie. **(B)** Same nomenclature as in A except that the preparation was exposed to 1 µM 5-HT for 5 min. A ST map created in the same manner as that in A shows clear evidence of asynchronous Ca^{2+} transients. This is more evident from examining the fluorescence intensity profile of the same two cells analyzed in A, which displayed repetitive Ca^{2+} transient of distinct magnitude and frequency. **(C)** The nomenclature of this panel is identical to that of B and C, with the exception that the PA was exposed to 10 µM $CaCC_{Inh}$-A01 for 10 min while still being incubated with 5-HT. Examination of the ST map reveals little, if any, Ca^{2+} oscillations in the presence of the ANO1 inhibitor; Ca^{2+} transients were no longer apparent in the same two cells analyzed in A and B.

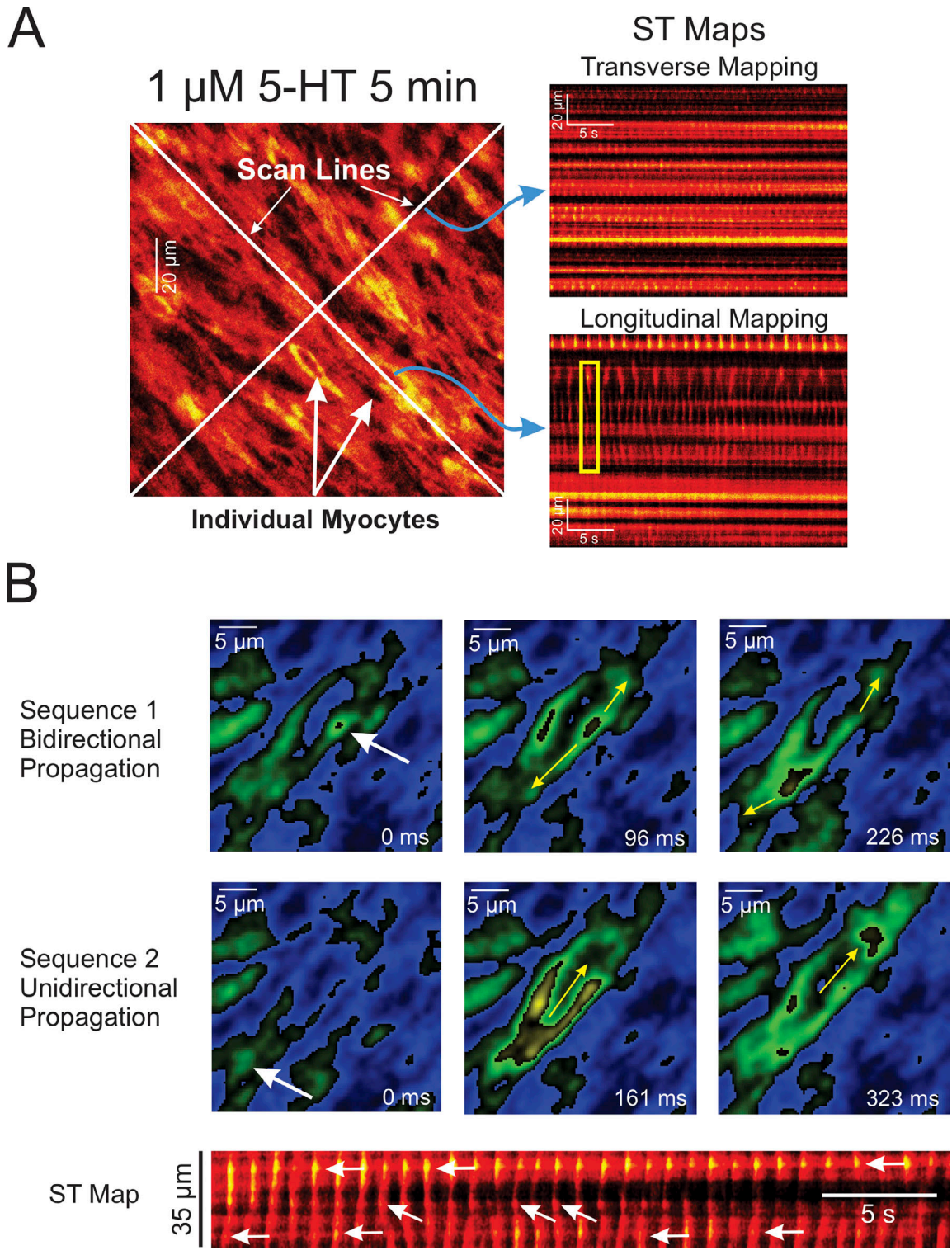

Figure 4. **Examples of asynchronous Ca^{2+} oscillations and waves in PASMCs from intact PAs from SMC-GCaMP3 mice. (A)** Examples of ST maps created by analyzing a video recorded from an intact endothelium-denuded PA from a SMC-GCaMP3 mouse exposed to 1 μM 5-HT for 5 min. The left larger image was extracted from a video stack onto which were drawn two white scan lines. The scan lines were oriented along or orthogonally to the main axis of the cells. The two images on the right show ST maps that were created by reporting fluorescence intensity registered under the scan line drawn orthogonally (Transverse Mapping) or along (Longitudinal Mapping) the main axis of the cells, respectively. The top ST map clearly shows a lack of cell-to-cell propagation of Ca^{2+} transients (bright luminous spots) in the transverse direction. Longitudinal mapping also suggests a lack of or poor evidence for propagation from one cell to the next along the main axis of the cells. Ca^{2+} transients propagated along the main axis of the cells (as evidenced from the near vertical streaks of fluorescence) but collapsed at the end of the cells, failing to propagate the signal to neighboring cells (one example highlighted by the yellow box). **(B)** Two series of images showing the initiation and propagation of two Ca^{2+} waves (top and bottom sets of images) taken at different times from the original movie. The white arrows show trigger sites. The yellow arrows illustrate the direction of propagation of the waves. The ST map at the bottom of the panel was reconstructed

from the entire video with time passing from left to right. The white arrows indicate the location of at least three trigger sites that initiated Ca^{2+} waves in this particular cell. The trigger sites randomly changed from either of the cell tips or the middle of the cell. Bidirectional propagation from the middle site is evident from the "V" shape appearance of these particular waves.

clustered in a limited number of specialized microdomains along the cell length to form a specialized unit optimized for EC coupling of PASMCs. To test this hypothesis, we performed co-IP assays complemented by colocalization studies by confocal and superresolution nanomicroscopy.

Co-IP studies

Immunoprecipitation of ANO1 from freshly prepared total lysates of mouse PA followed by probing with $Ca_V1.2$ and IP_3R antibodies, respectively, detected a high molecular weight band consistent with $Ca_V1.2$ (>250 kD) and several bands ≥100 kD for IP_3R (~240, 180, and 120 kD) in the immunoprecipitated macromolecular complex (Fig. 8, A and B). Of the three IP_3 bands, the higher one appears the most likely candidate for IP_3R as all three isoforms have a molecular weight >200 kD (Monkawa et al., 1995). Input from total PA lysate (10%) detected the same immunoreactive bands for $Ca_V1.2$ and IP_3R. A band near the size predicted (~110 kD) for ANO1 monomeric protein was also detected from the immunoprecipitated complex, which could not be achieved when total lysates were directly probed by Western blot with the same ANO1 antibody, most likely attributable to the low abundance of ANO1 protein in PA tissue (data not shown). These results support the notion that cortical IP_3R and $Ca_V1.2$ reside in the same membrane fraction as ANO1.

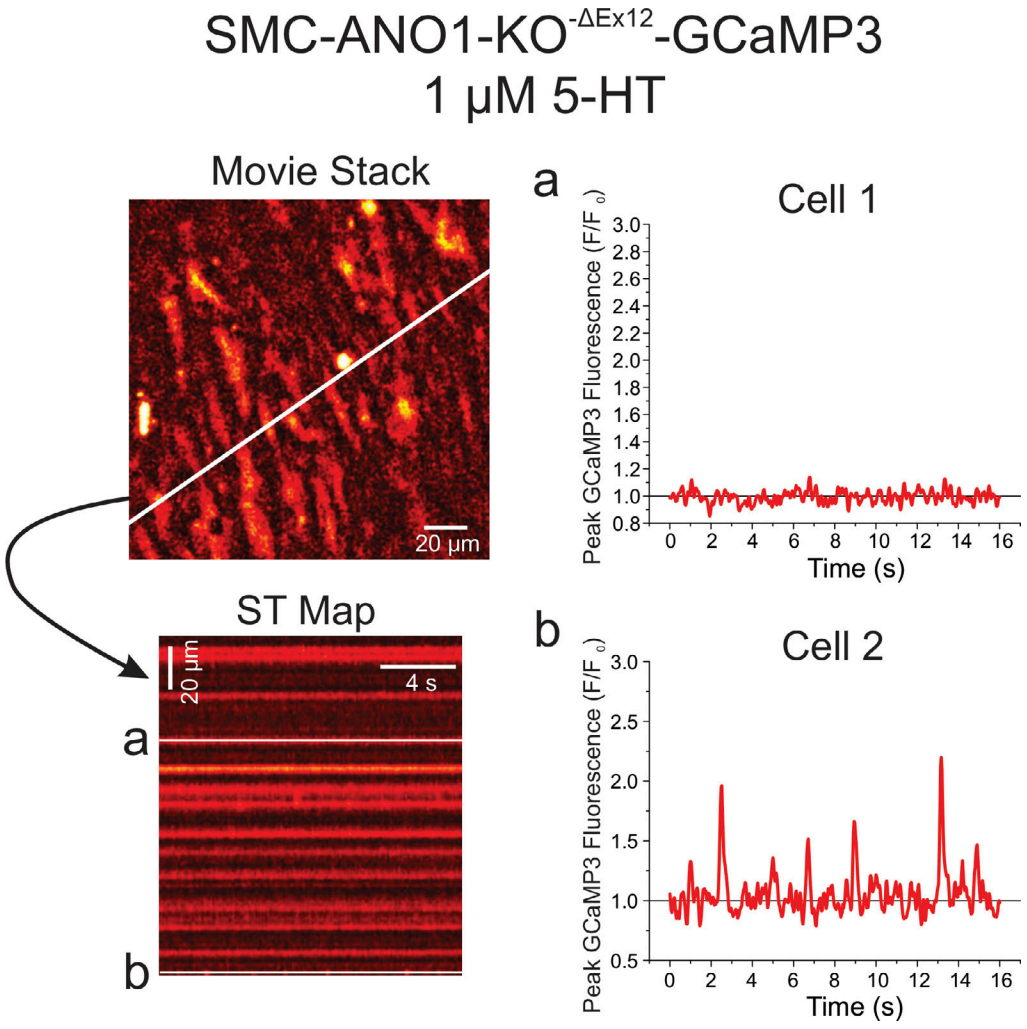

Figure 5. **Sample experiment illustrating how ANO1 knockdown exerted a strong inhibition of 5-HT-induced Ca^{2+} oscillations in a PA from a tamoxifen-injected SMC-ANO1-KO-$^{\Delta Ex12}$-GCaMP3 mouse.** The top left panel is an image from a video stack recorded in a pulmonary artery from a conditional smooth muscle cell-specific and inducible ANO1 knockout mouse expressing GCaMP3 specifically in smooth muscle cells, which was exposed to 1 μM 5-HT for 5 min. One ST map constructed from the white line crossing the image is shown in the lower left corner and reveals very little activity. The fluorescence intensity profile as a function of time of two cells from the ST map labeled with the letters a and b are shown on the right. Cell 1 displayed no significant Ca^{2+} activity while Cell 2 showed low-frequency Ca^{2+} events.

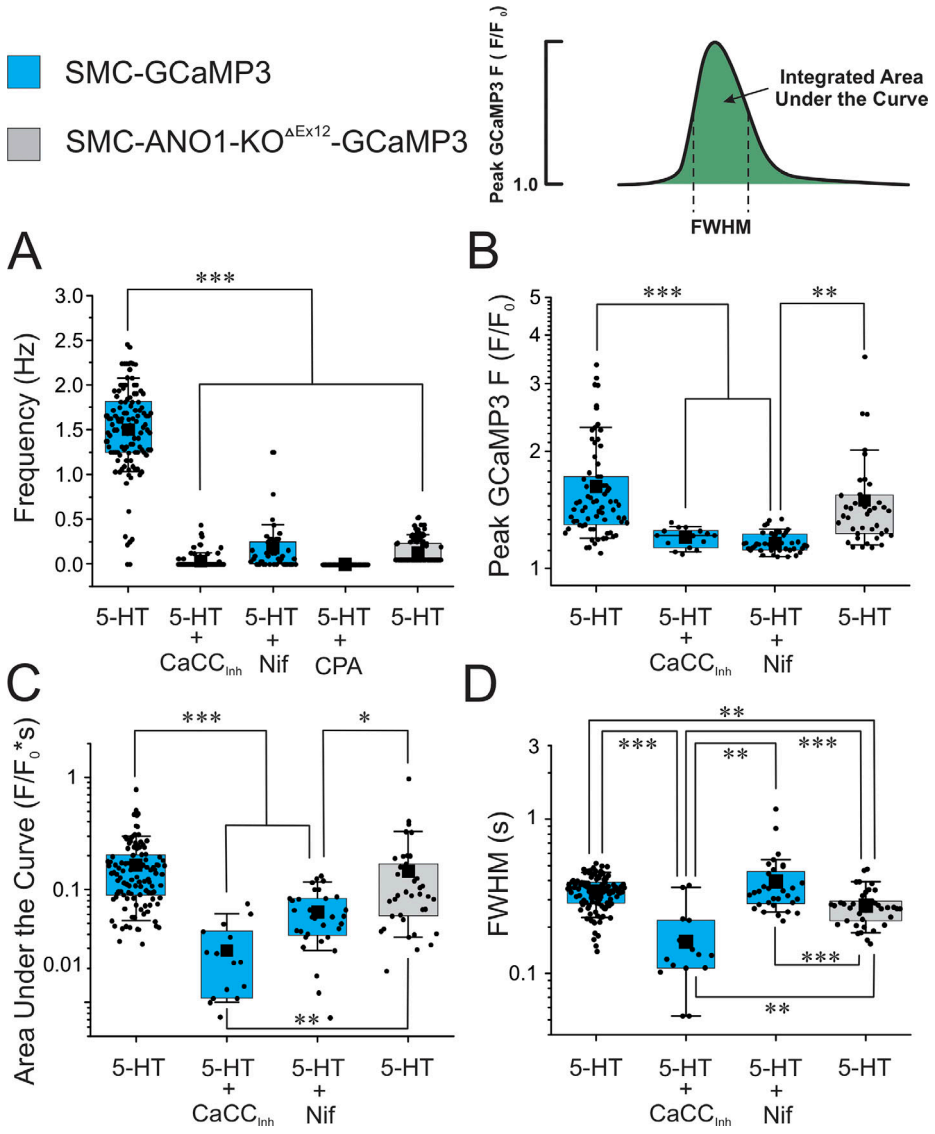

Figure 6. **Asynchronous Ca^{2+} oscillations evoked by 5-HT require both functional ANO1 and VGCC.** Mean data for each of four parameters measured from Ca^{2+} transients elicited by 1 µM 5-HT (5 min) in PA from control SMC-GCaMP3 (light blue bars) or SMC-ANO1-KO-$^{\Delta Ex12}$-GCaMP3 (light gray bars) mice. **(A–D)** The frequency of Ca^{2+} oscillations (A), peak Ca^{2+} transient amplitude (F/F_0; B), integrated area under the curve (C), and FWHM (D) were measured as shown in the upper right corner. For each dataset, the mean is indicated by a filled black square with the colored boxes and whiskers delimiting the 25th and 75th percentile, and the 10th and 90th percentile of the pooled data, respectively, and small dots individual data points. *N*: number of animals; *n*: number of cells. SMC-GCaMP3 + 5-HT: $N = 7$, $n = 114$ for peak, area under the curve, and FWHM, and $n = 116$ for frequency; SMC-GCaMP3 + 5-HT + $CaCC_{Inh}$-A01 ($CaCC_{Inh}$): $N = 7$, $n = 15$ for peak, area under the curve, and FWHM, and $n = 76$ for frequency; SMC-GCaMP3 + 5-HT + nifedipine (Nif): $N = 2$, $n = 32$ for peak, area under the curve, and FWHM, and $n = 47$ for frequency; GCaMP3 + 5-HT + CPA: $N = 2$, $n = 29$; SMC-ANO1-KO-$^{\Delta Ex12}$-GCaMP3; 5-HT: $N = 7$, $n = 39$ for peak, area under the curve, and FWHM, and $n = 137$ for frequency. For all panels, ***, **, and * indicate a significant difference between means with $P < 0.001$, $P < 0.01$, and $P < 0.05$, respectively.

Peripheral distribution of ANO1, $Ca_V1.2$, and IP_3R in PASMCs

Laser scanning confocal fluorescence microscopy was first used to visualize mouse PASMCs dually immunolabeled for ANO1 and $Ca_V1.2$, or ANO1 and IP_3R. Both protein pairs demonstrated a preferential colocalization near the PM of PASMCs although significant immunolabeling of IP_3R was also apparent in the cytosol as expected for a protein expressed in the SR (Fig. 8, C and E). Line plots of normalized fluorescence intensity of regions indicated by the dashed white lines in Fig. 8, D and F, show an excellent correlation of fluorescence intensity near the PM between ANO1 and $Ca_V1.2$ (Fig. 8 D), and between ANO1 and IP_3R (Fig. 8 F), albeit significant labeling for IP_3R was apparent intracellularly as expected.

Nanoscale colocalization of ANO1 with $Ca_V1.2$ and IP_3R in PASMCs

We further investigated the colocalization of ANO1 with $Ca_V1.2$ and IP_3R protein clusters at nanoscale resolution (<40 nm) using GSDIM (ground-state depletion followed by individual molecule return)superresolution microscopy. Mouse PASMCs were dually immunolabeled in pairs either with ANO1 versus $Ca_V1.2$ or ANO1 versus IP_3R and imaged in either epifluorescence illumination mode or TIRF mode using GSDIM. Superresolution

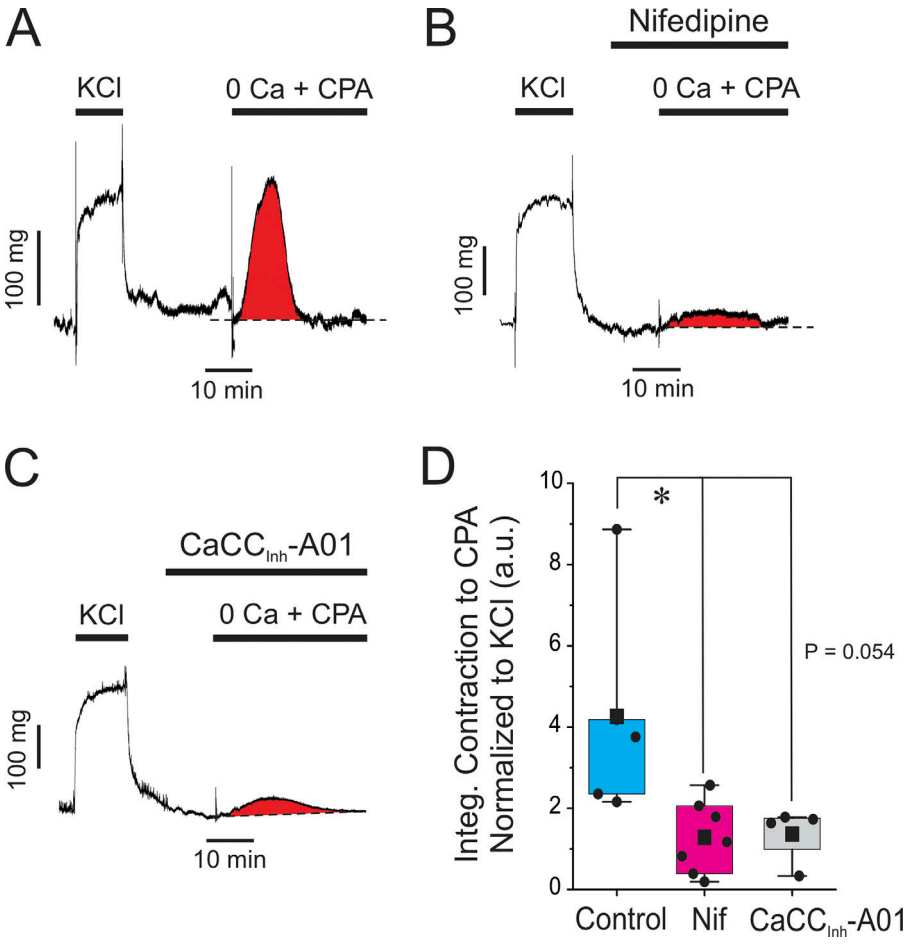

Figure 7. **Blocking ANO1 or $Ca_V1.2$ depletes SR Ca^{2+} stores. (A)** Typical isometric force recording obtained under control conditions showing the effect of depleting the SR Ca^{2+} stores. After eliciting a sustained contraction with high K^+ (KCl; 85.4 mM), the preparation was switched to normal Krebs for 20 min, which relaxed the artery to baseline. The solution was subsequently changed to a Ca^{2+}-free Krebs solution containing 100 µM EGTA and 10 µM cyclopiazonic acid (0 Ca + CPA), which triggered a transient contraction produced by releasing Ca^{2+} from internal SR Ca^{2+} stores. The area under the curve for the transient contraction highlighted in red was measured and used as an index of the amount of Ca^{2+} stored in the SR. **(B and C)** Similar experiments to that shown in A, with the exception that each preparation was incubated for 10 min with 1 µM nifedipine or 10 µM $CaCC_{Inh}$-A01, respectively, prior to switching to the Ca^{2+}-free solution with CPA in the presence of either drug. Both compounds exerted a strong inhibition of the transient contraction elicited by CPA as evident from the much reduced area under the curve shown in red. **(D)** Pooled data from similar experiments are shown in A–C. For each dataset, the mean is indicated by a filled black square with the colored boxes and whiskers delimiting the 25th and 75th percentile, and the 10th and 90th percentile of the pooled data, respectively, and small dots individual data points of the integrated contraction measured in the presence of 0 Ca + CPA, normalized to the KCl-induced contraction (a.u.: arbitrary unit). Control, $N = 5$; nifedipine, $N = 7$; $CaCC_{Inh}$-A01, $N = 4$; * indicates a significant difference between means with $P < 0.05$. The comparison between the Control and $CaCC_{Inh}$-A01 groups was just at the limit of significance as shown.

images were created using the ImageJ plugin ThunderSTORM. In the epifluorescence mode of acquisition, molecules could be visualized close to the periphery (Fig. 9, A and B), especially for the ANO1-$Ca_V1.2$ pairing. We used the ThunderSTORM coordinate-based colocalization (CBC) algorithm to quantify the spatial correlation of the proteins where the single-molecule localizations (SML) for each protein pair are given a value of −1 to 1, where −1 is anticorrelated, 0 suggests a random distribution with respect to each other, and 1 is highly correlated. We found that the highest percentage of localizations for ANO1-$Ca_V1.2$ in epifluorescence mode were within the range of 0.9–1, demonstrating a high degree of correlation (Fig. 9 C). The CBC value for IP_3R was not as high albeit significant due to the presence of intracellular IP_3R proteins (Fig. 9 D), which would be expected for a protein localized to the SR. We next imaged the protein pairs using TIRF mode, allowing us to determine the distance between the protein pairs at the periphery of the cell with high resolution. We determined the nearest neighbor distance for each protein pair based on the single-molecule distributions of localizations for each protein. Here, we found that both $Ca_V1.2$ and IP_3R are located closer to ANO1 than randomly localized particles (Fig. 9 G).

Analysis of the size and density of clusters

Using the program SR-Tesseler approach (Levet et al., 2015), we investigated the clustering of the molecules on or near the PM. The localization data from the TIRF-based SMLs were subdivided using Voronoï tessellation (or segmentation), which creates polygonal regions around each point that is equidistant from surrounding localizations, as demonstrated in Fig. 9 H, top panel. Parameters such as area, density, and mean distance to the surrounding polygons are used to determine areas of higher molecular densities. Using this method, we measured the size of clusters that had a density 2.5 times greater than the average molecule density. Examples of identified clusters are shown in Fig. 9 H, bottom panel, with the polygons that were included in the cluster identified in yellow, and the shape of the identified clusters are shown by the red line. All three protein cluster sizes similarly ranged from <50 to >5,000 nm^2, with the majority of clusters ranging from 100 to 500 nm^2 (Fig. 9 I). Taken together, these results indicate that ANO1 and $Ca_V1.2$, and ANO1 and IP_3R, colocalize in microdomains of similar sizes in specific areas near the PM of PASMCs, which may be optimally organized for effective agonist-mediated Ca^{2+} signaling.

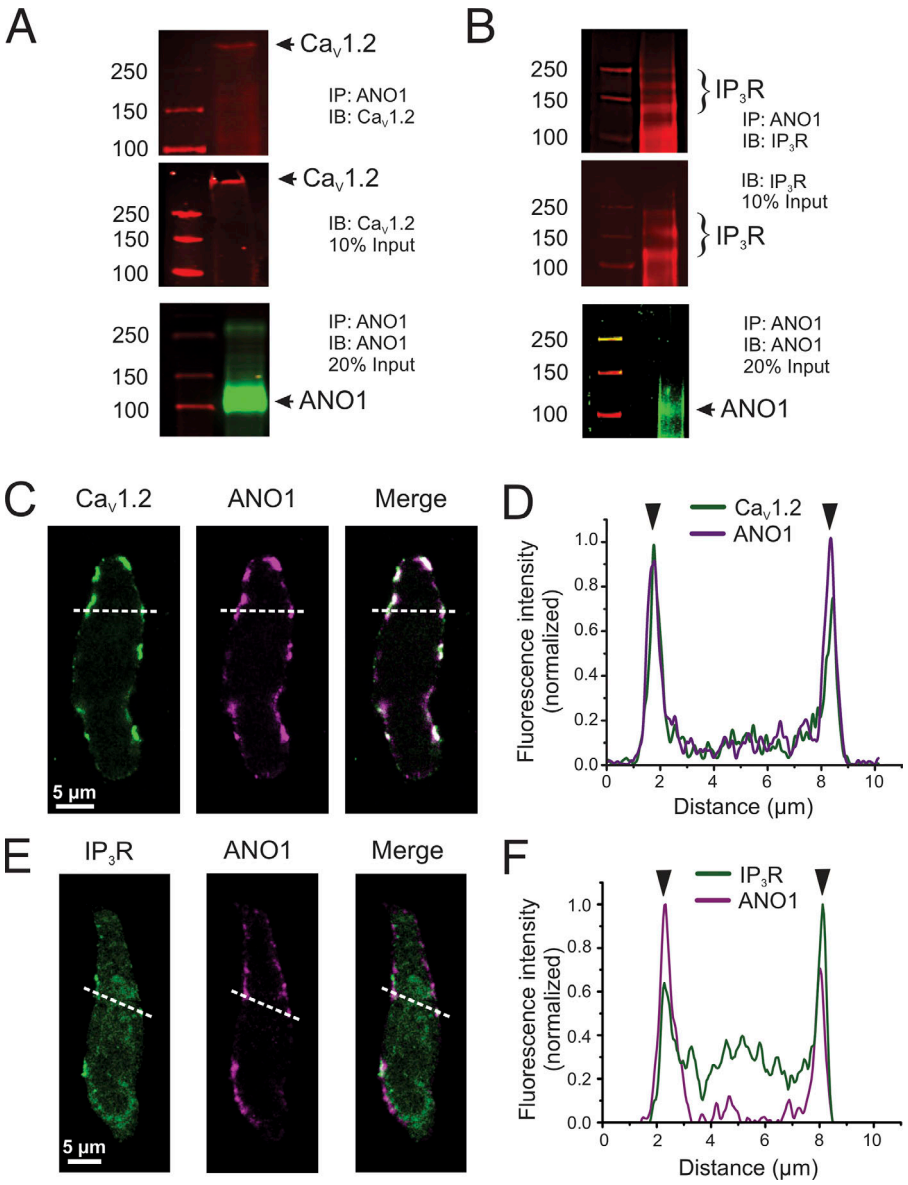

Figure 8. **ANO1, $Ca_V1.2$, and IP_3R colocalize in peripheral coupling sites to form signaling complexes. (A and B)** Co-IP of $Ca_V1.2$ or IP_3R with ANO1 from lysates of the pulmonary artery from wild-type mice. Pulldown was carried out with anti-ANO1 antibody and then probed by Western blot with anti-$Ca_V1.2$, anti-IP_3R, or anti-ANO1 antibodies. Five to six mouse tissues per experiment, each ran in triplicates. **(C and D)** Freshly isolated PASMCs from wild-type mice were immunolabeled for ANO1 and $Ca_V1.2$ (C) or ANO1 and IP_3R (D). All three proteins were preferentially localized to the periphery of the cells. **(D and F)** Line profiles of the areas indicated by the white dashed lines in C and E. The fluorescence intensity was normalized to the minimum and maximum fluorescence for each sample. The black arrowheads denote the location of the PM. ANO1 and $Ca_V1.2$ show strong immunolabeling at the PM (D). **(E)** IP_3R shows some intracellular immunolabeling, with moderate peaks present at the periphery showing an enhancement of protein localization to peripheral coupling sites. Source data are available for this figure: SourceData F8.

Disruption of lipid rafts eliminates PM ion channel super clusters and inhibits 5-HT-mediated EC-coupling

The results presented above suggest that unique coupling sites at the PM of PASMCs are important for G_q-protein receptor-mediated EC coupling. We hypothesized that these structural microdomains may be intimately associated with lipid rafts, and perhaps with caveolae, a subset of lipid rafts, which are known to be involved in sequestering membrane receptors and ion channels for optimal compartmentalized signal transduction (Patel et al., 2008; Thomas and Smart, 2008; Guéguinou et al., 2015). This is also based on previous reports showing that both ANO1 and $Ca_V1.2$ are localized in caveolae (Jorgensen et al., 1989; Darby et al., 2000; Löhn et al., 2000; Sones et al., 2010). Fig. 10, A–D shows the effect of incubating wild-type PASMCs for 30 min with 3 mg/ml methyl-β-cyclodextrin (MβCD) on the cellular distribution of ANO1 and $Ca_V1.2$. MβCD causes membrane cholesterol depletion, which disrupts lipid rafts and caveolae (Rodal et al., 1999; Zidovetzki and Levitan, 2007; Patel et al., 2008). The PASMCs shown in Fig. 10, A and C, were isolated from the same animal. Similar to the results presented in Fig. 6, ANO1 and $Ca_V1.2$ displayed strong PM colocalization (Fig. 10, A and B) as probed by confocal microscopy. As anticipated, exposure to MβCD resulted in the disappearance of the ANO1/$Ca_V1.2$ superclusters and caused significant internalization of both proteins (Fig. 10, C and D). We quantified in PASMCs from three mice the redistribution of ANO1 and $Ca_V1.2$ by measuring the ratio of the membrane to total cell fluorescence. MβCD caused a 31.5% and 31.0% reduction in this parameter for ANO1 (Fig. 10 E) and $Ca_V1.2$ (Fig. 10 F), respectively, indicating that membrane cholesterol depletion produced a quantitatively similar effect on both proteins.

We next examined the functional significance of disrupting lipid rafts on 5-HT receptor-mediated signaling in intact PA. Exposing arteries to MβCD caused a similar decrease in the

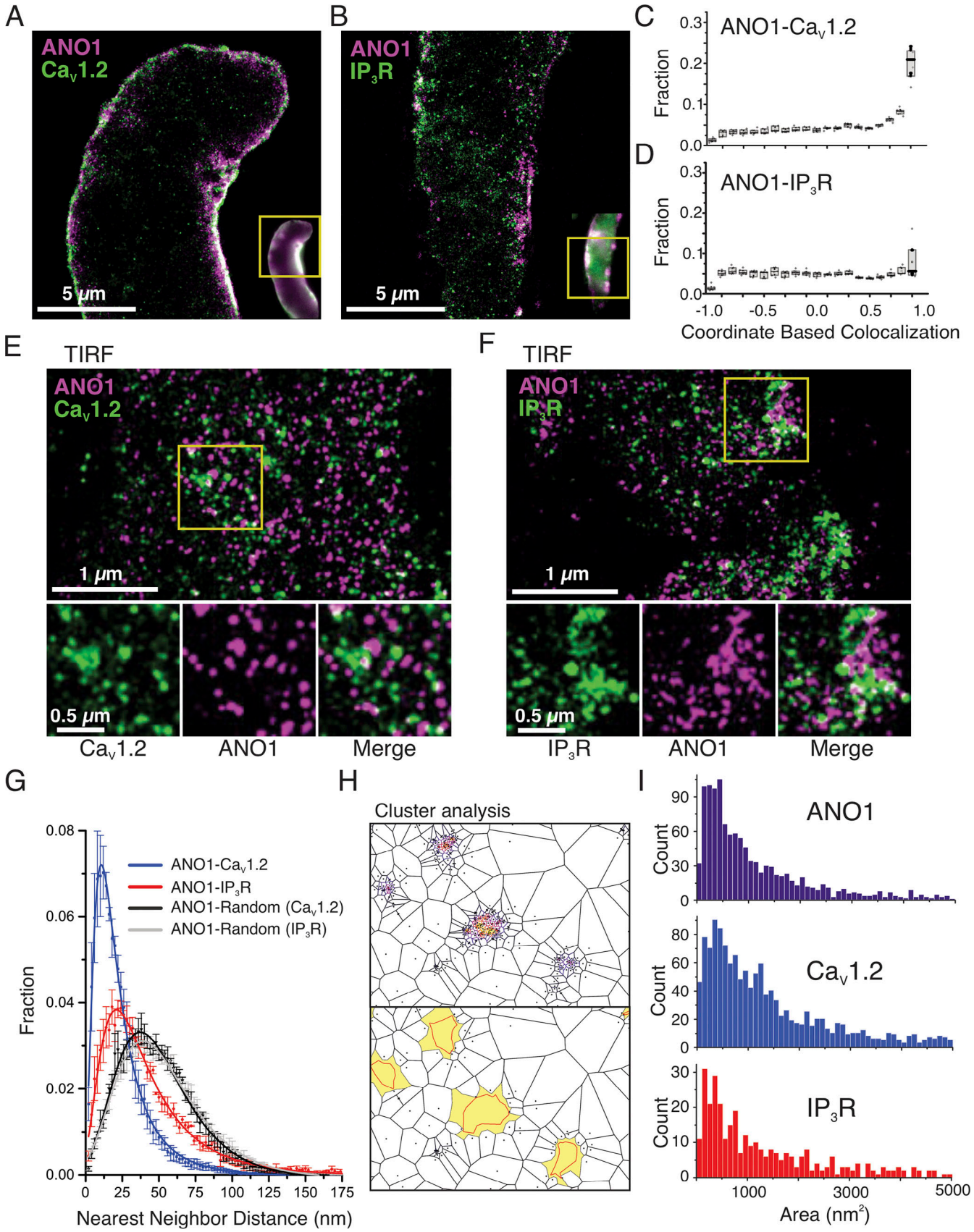

Figure 9. **Superresolution imaging of ANO1, $Ca_V1.2$, and IP_3R at the PM of PASMCs from wild-type mice. (A and B)** Superresolution images of PASMCs labeled for ANO1 and $Ca_V1.2$ (A) or ANO1 and IP_3R (B) were imaged using GSDIM in epifluorescence mode. Epifluorescence images are shown in the inset for

reference, with the yellow box demonstrating the region for GSD imaging. **(C and D)** Coordinate-based colocalization (CBC) of ANO1-$Ca_V1.2$ (C) or ANO1 and IP_3R (D) where −1 shows mutual exclusion and +1 shows high correlation. **(E and F)** Superresolution images of PASMCs labeled with ANO1 and $Ca_V1.2$ (E) or ANO1 and IP_3R (F) were imaged using GSDIM in TIRF mode. Enlargements of the white boxes are shown to the right, highlighting the adjacent location of the protein pairs. **(G)** Nearest neighbor analysis of the protein pairs demonstrates that the single-molecule localizations of $Ca_V1.2$ (blue) and IP_3R (red) are both located closer to ANO1 than would be expected for a randomly distributed protein (black and grey). **(H)** An example of Voronoï-based segmentation of $Ca_V1.2$ single-molecule localizations (top) and the corresponding identified clusters are shown in yellow with the outline of the identified clusters denoted by the red line (bottom). **(I)** Cluster sizes of ANO1 (top), $Ca_V1.2$ (middle), and IP_3R (bottom) as determined using SR-Tesseler analysis as shown in H.

contraction to 5-HT as that produced by either $CaCC_{Inh}$-A01 or CPA (both datasets reproduced from Fig. 1 A). In contrast, the contraction amplitude triggered by high K^+ (85.4 mM) was not significantly different between control and MβCD-treated arteries (data not shown; Control: 0.25 ± 0.04 g, n = 10; MβCD: 0.27 ± 0.03 g, n = 5; P > 0.05). These results indicate that the reduction of the 5-HT-induced contraction caused by MβCD was not due to an inability of intact PA to contract to a depolarizing stimulus. We next investigated how the same treatment would influence Ca^{2+} signaling evoked by 5-HT in intact PA from SMC-GCaMP6f mice. Consistent with the contraction data, MβCD (3 mg/ml for 30 min) significantly reduced the frequency (Fig. 11 B), amplitude (Fig. 11 C), the area under the curve (Fig. 11 D), and duration (Fig. 11 E) of GCaMP6f Ca^{2+} transients. These results indicate that the destruction of ANO1 and $Ca_V1.2$ coupling sites on the PM by MβCD had a major disrupting impact on the ability of 5-HT to trigger Ca^{2+} oscillations and force production.

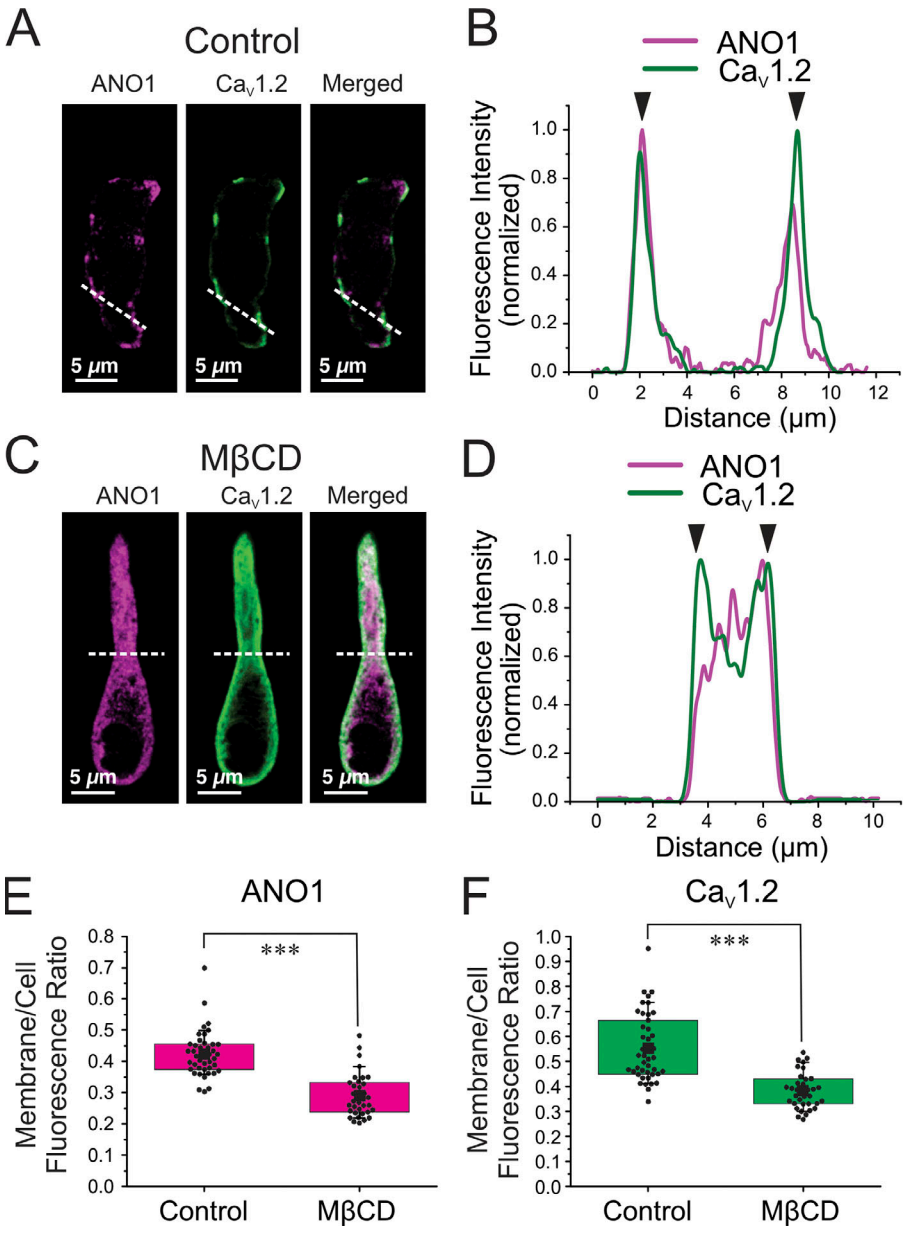

Figure 10. **Membrane cholesterol depletion with MβCD causes the internalization of ANO1 and $Ca_V1.2$ proteins. (A and C)** Freshly isolated PASMCs from wild-type mice were immunolabeled for ANO1 and $Ca_V1.2$ before (A) or after (C) a 30-min exposure to MβCD (3 mg/ml; MβCD) to deplete membrane cholesterol and disrupt lipid rafts. The two ion channel proteins were preferentially localized to the periphery of the cells in control conditions as similarly shown in Fig. 8. **(B–D)** Line profiles of the areas indicated by the white dashed lines in A and C are respectively displayed in B and D. For these plots, the fluorescence intensity was normalized to the minimum and maximum fluorescence for each sample. The black arrowheads denote the location of the PM. ANO1 and $Ca_V1.2$ show strong immunolabeling at the PM in control condition (C) and translocation toward the center core of the cell after exposure to MβCD (D). The cells from A and C were isolated from the same mouse. **(E and F)** Graphs summarizing the effects of exposing PASMCs to MβCD on the distribution of ANO1 (magenta bars) and $Ca_V1.2$ (green bars), respectively. Measurements were performed as described in the text and consisted in normalizing membrane fluorescence to total cell fluorescence. For each dataset, the mean is indicated by a large, filled black square with the colored boxes and whiskers delimiting the 25th and 75th percentile, and the 10th and 90th percentile of the pooled data, respectively, and small dots individual data points. N: number of animals; n: number of cells; for the control group (E): ANO1 and $Ca_V1.2$: N = 3, n = 43; for the MβCD group (F): ANO1 and $Ca_V1.2$: N = 3, n = 35. *** indicates a significant difference between means with P < 0.001.

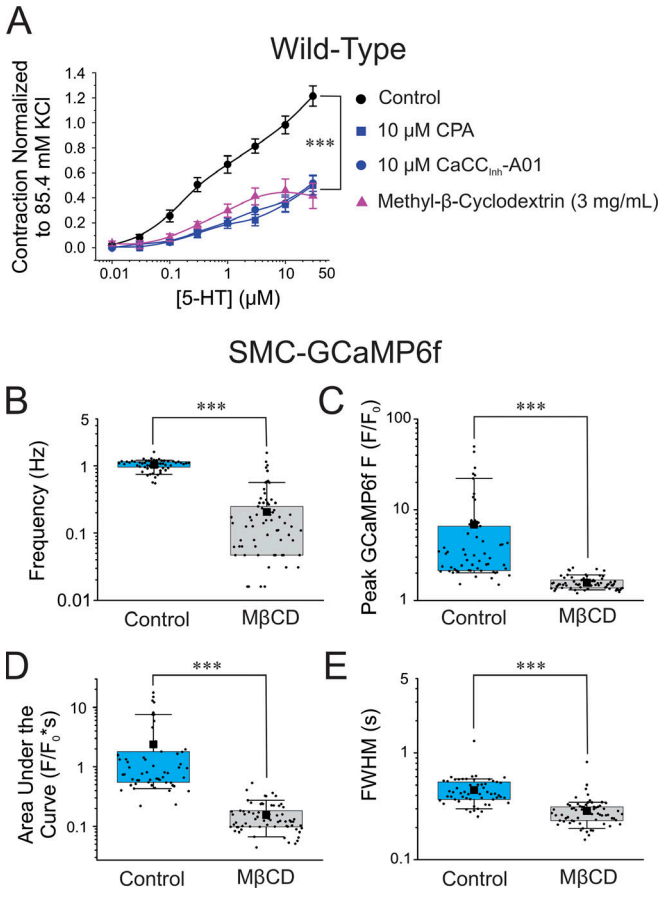

Figure 11. **Disruption of lipid rafts with MβCD inhibits EC coupling mediated by 5-HT. (A)** Mean cumulative dose–response curves to 5-HT in mouse pulmonary arteries from wild-type C57/BL6 mice in control condition (black circles, Control; *N* = 14), a 10-min exposure to 10 μM CPA (blue squares; *N* = 4), a 10-min exposure to 10 μM CaCC$_{Inh}$-A01 (blue circles; *N* = 6), or after a 30-min incubation with MβCD (3 mg/ml) to deplete membrane cholesterol and disrupt lipid rafts (upper triangles; *N* = 5). The data for the control, CPA, and CaCC$_{Inh}$-A01 groups were reproduced from Fig. 1 B to facilitate comparisons. Each data point is a mean ± SEM of net contractile force normalized to the second high K$^+$–Krebs solution-induced contraction (see description in Materials and methods). **(B–E)** The summarized data presented in B–E show the effects of exposure of pulmonary arteries from conditional and smooth muscle-specific GCaMP6f mice (SMC-GCaMP6f) to a 30-min exposure with 3 mg/ml of MβCD on the frequency of GCaMP6f Ca^{2+} oscillations (B; Control, *n* = 58; MβCD, *n* = 78), peak GCaMP6f Ca^{2+} transients (C; Control, *n* = 58; MβCD, *n* = 70), area under the curve of GCaMP6f Ca^{2+} transients (D; Control, *n* = 58; MβCD, *n* = 70) and FWHM GCaMP6f Ca^{2+} transients (E; Control, *n* = 58; MβCD, *n* = 70). The Control (light blue boxes) and MβCD (light gray boxes) datasets in B–F are from the same animals (*N* = 4). For each dataset in the latter panels, the mean is indicated by a filled black square with the colored boxes and whiskers delimiting the 25th and 75th percentile, and the 10th and 90th percentile of the pooled data, respectively, and small dots individual data points. For all panels, *** indicates a significant difference between means with P < 0.001.

Discussion

We have demonstrated that the contribution of ANO1 to agonist-mediated signaling in mouse PASMCs is more complex than that predicted from the simple working model of a widespread and uniform positive feedback loop between Ca^{2+} entry through VGCC and the sustained membrane depolarization caused by Ca^{2+} activation of ANO1 (Fig. 12 A). Instead, we conclude that the fraction of the contraction to 5-HT that is membrane potential-dependent requires the coordinated interaction of ANO1, Ca$_V$1.2, and IP$_3$R colocalized in a finite number of superclusters spread across the cell length (Fig. 12 B). This interaction is responsible

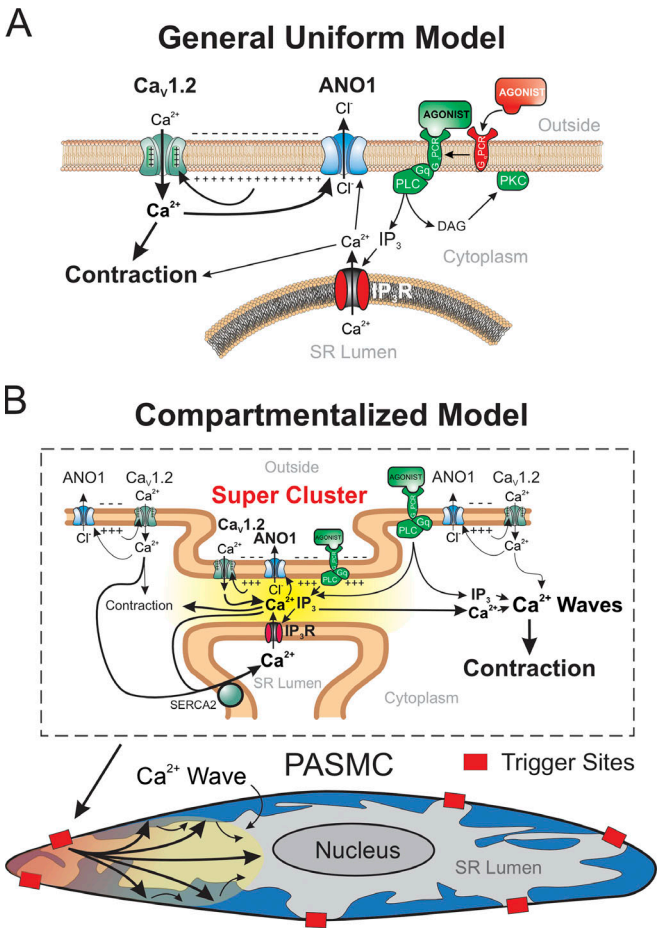

Figure 12. **Hypothetical models of EC coupling involving ANO1, Ca$_V$1.2, and IP$_3$R during agonist-mediated contraction of mouse pulmonary arterial smooth muscle cells. (A)** General uniform model depicting the activation of ANO1 by both Ca^{2+} release from IP$_3$-sensitive SR Ca^{2+} stores and Ca^{2+} entry through Ca$_V$1.2. In this model, the three ion transporters are evenly distributed in the membrane and are not physically coupled. The depolarization is maintained by the positive feedback loop established by Ca$_V$1.2-mediated activation of Cl^- efflux through ANO1 and its impact on the state of activation of Ca$_V$1.2 through regulation of membrane potential. **(B)** Schematic diagram illustrating the local interaction of ANO1, Ca$_V$1.2 with IP$_3$R and their impact on membrane potential, Ca^{2+} entry, and contraction. In this model, the three ion channels are physically coupled in a restricted number of sites (Super Cluster) distributed across the long axis of the cell (shown as red boxes in the bottom diagram) and are organized for compartmentalized Ca^{2+} signaling as highlighted by the yellow gradient area between the PM and segments of the SR in the close vicinity of the PM (top diagram). These compartmentalized areas serve the role of trigger sites for initiating Ca^{2+} waves that can then propagate through Ca^{2+}-induced Ca^{2+} release (CICR). Ca^{2+} entry through Ca$_V$1.2, which is maintained by the depolarization caused by ANO1, supports the microenvironment that is necessary to promote the propagation of the Ca^{2+} waves by CICR and to reload SR Ca^{2+} stores. PASMC: pulmonary artery smooth muscle cell; IP$_3$: inositol-triphosphate; G$_q$PCR: G$_q$-protein coupled receptor; PLC: phospholipase C; SERCA2: type 2 Ca^{2+}-ATPase of the SR.

for evoking and sustaining intracellular Ca^{2+} oscillations that propagate along the main axis of the cell, with little evidence for cell-to-cell transmission. Our data are consistent with previous reports showing that 5-HT or endothelin-1 triggered asynchronous Ca^{2+} oscillations in small arteries and arterioles of mouse lung slices (Perez and Sanderson, 2005; Perez-Zoghbi and Sanderson, 2007). Simultaneous measurements of Ca^{2+} transients and changes in luminal size, as an index of constriction, showed that the force of arteriolar contraction to agonists mainly depends on the frequency of Ca^{2+} oscillations. The observation that the constriction produced by agonists is sustained and non-oscillatory is hypothesized to be caused by the summation in space and time of force produced by individual myocytes and the fact that muscle relaxation is much slower than the Ca^{2+} transients triggering force production (Perez and Sanderson, 2005).

A remarkable observation of the present study was the similar inhibitory effectiveness of suppressing ANO1, VGCC, or Ca^{2+} release from the SR on the contraction to 5-HT. These results suggest that the contraction requires all three elements to maintain force production. This is supported by Ca^{2+} imaging experiments showing that similar treatments strongly inhibited or abolished Ca^{2+} oscillations in myocytes from intact pulmonary arteries of mice conditionally expressing the Ca^{2+} biosensor protein GCaMP3 in smooth muscle cells. We hypothesize that cyclical Ca^{2+} release from IP_3R triggers self-regenerative Ca^{2+} waves that propagate along the long axis of the cell through Ca^{2+}-induced Ca^{2+} release. Whether this process also involves ryanodine (RyR) receptor-sensitive SR Ca^{2+} pools is unclear. Some studies found no role for RyR in response to agonists (Hamada et al., 1997; Hyvelin et al., 1998; Zheng et al., 2005; Henriquez et al., 2018), while a few others revealed a significant contribution of RyR and crosstalk between RyR- and IP_3R-sensitive Ca^{2+} pools (Yang et al., 2005; Clark et al., 2010).

Although ANO1, $Ca_V1.2$, and IP_3R are required for maintaining a stable contraction, propagated SR Ca^{2+} release through IP_3R is probably the main factor involved in this process because (1) SR Ca^{2+} depletion obliterated Ca^{2+} oscillations, whereas inhibition of $Ca_V1.2$ or ANO1 reduced but did not abolish Ca^{2+} transients; and (2) blocking SR Ca^{2+} release by SR Ca^{2+} depletion or blocking specifically IP_3R with xestospongin C reduced the amount of force to the same extent, if not more, than inhibiting Ca^{2+} entry through $Ca_V1.2$ or preventing the depolarization driven by ANO1. There is a possibility that SOCE might have been involved in the remaining contraction to 5-HT following SR Ca^{2+} depletion or inhibition of $Ca_V1.2$ or ANO1, but this Ca^{2+} entry pathway was likely a minor contributor in our conditions using healthy untreated mice (Ng et al., 2007; Liu et al., 2012), as opposed to its significant enhancement in preparations from animals with PH (Lin et al., 2004; Liu et al., 2012; Xia et al., 2014). Consistent with this idea were the observations that removing extracellular Ca^{2+} in the presence or absence of CPA produced similar results.

Since the membrane phospholipid PIP_2 is the precursor of IP_3 during the activation of 5-HT receptors and G_q-protein, the ensuing depletion of PIP_2 is likely to affect the contractile and Ca^{2+} signaling responses described in the PIP_2 study. PIP_2 is required to maintain the activity of voltage-gated Ca^{2+} channels (Wu et al., 2002; Gamper et al., 2004; Suh et al., 2012). For reasons that are unclear, PIP_2 was shown to inhibit ANO1-encoded native CaCCs in vascular smooth muscle cells in one study (Pritchard et al., 2014), while several more recent studies revealed that it either upregulated or was required to support the activity of cloned ANO1 expressed in mammalian cell lines (Ta et al., 2017; Le et al., 2019, 2021; Tembo et al., 2019; Jia and Chen, 2021; Ko and Suh, 2021). The overall impact of the regulation of $Ca_V1.2$ and ANO1 by PIP_2 on EC coupling in PASMCs thus remains unclear but will be important to consider in future investigations.

If Ca^{2+} release from IP_3R-sensitive SR pools is the main driver of Ca^{2+} oscillations and contraction, then what is the role of ANO1 and $Ca_V1.2$ in this pathway? It is possible that their interaction causes a small but significant elevation in resting $[Ca^{2+}]_i$ that would produce two effects of functional significance: (1) it would increase the probability of triggering an intracellular Ca^{2+} wave, especially at supercluster sites (see discussion below), by lowering the threshold for IP_3 to open IP_3Rs (Berridge et al., 2000; Berridge, 2009; Woll and Van Petegem, 2022); and (2) it would promote the refilling of Ca^{2+} stores via enhanced SERCA activity (Berridge et al., 2000; Berridge, 2009; Woll and Van Petegem, 2022), which would increase the activity of Ca^{2+} release channels through their dependence on luminal Ca^{2+} levels (Györke and Györke, 1998; Berridge et al., 2000; Berridge, 2009; Woll and Van Petegem, 2022). This hypothesis is consistent with the observation that Ca^{2+} oscillations were shown to persist for a short time period in the absence of extracellular Ca^{2+} but they eventually subsided due to depletion of Ca^{2+} stores (Perez and Sanderson, 2005; Perez-Zoghbi and Sanderson, 2007). In our study, blocking either $Ca_V1.2$ or ANO1 after a loading period with high K^+ solution produced a similar depletion of SR Ca^{2+} stores as indirectly assessed by measuring the transient contraction elicited by blocking SERCA in the absence of external Ca^{2+}. This observation supports the hypothesis that the main function of ANO1 and $Ca_V1.2$ mouse pulmonary arteries stimulated by 5-HT is to refill SR Ca^{2+} stores.

The close functional relationship between ANO1, $Ca_V1.2$, and IP_3R prompted us to examine whether these ion transporters display physical coupling bearing significance to agonist-induced EC coupling. Both $Ca_V1.2$ and IP_3R coimmunoprecipitated with ANO1 in pulldown assays. Confocal imaging experiments supported the notion of colocalization of the ANO1-$Ca_V1.2$ and ANO1-IP_3R protein pairs at or near the PM. Superresolution fluorescence nanomicroscopy (d-STORM) experiments in both epifluorescence and TIRF modes confirmed that some areas of the PM exhibit a high degree of correlation between ANO1 and $Ca_V1.2$ with many clusters showing the nearest neighbor distribution within a few tens of nanometers. This was also observed for ANO1-IP_3R protein pairs albeit to a lesser degree than for ANO1 and $Ca_V1.2$, which is to be expected considering that IP_3R are intracellular proteins located in the SR, but with some segments of this organelle making close contacts (~50 nm or less) with certain areas of the PM, i.e., SR/PM junctions, to fulfill highly localized functions (e.g., amplified or attenuated signal transduction, superficial buffer barrier function, SOCE;

Chen et al., 1992; van Breemen et al., 1995; Janssen et al., 1999; Jaggar et al., 2000; Liao et al., 2008, 2009; McElroy et al., 2008; Lee et al., 2010; Madl et al., 2010; Wang et al., 2017). An analysis of randomized distributions of the same fluorescent particles led to a doubling or more of the distance between the nearest neighbor pairs. Finally, cluster size distributions of the protein pairs, i.e., ANO1/$Ca_V1.2$ and ANO1/IP_3R were also remarkably similar, suggesting that the three proteins were colocalized in the same super clusters and overlapped. Triple labeling would have been ideal but could not be performed because the antibodies used to immunolabel $Ca_V1.2$ and IP_3R were both from a mouse, which would have required the choice and validation of another antibody for one of the two species. Nevertheless, these results suggest that the molecular assembly of the ANO1 PM/SR nanodomain is a coordinated process leading to a unique physical association between the three ion channel proteins that are designed to amplify local Ca^{2+} signaling for optimal development of force.

A tight physical coupling between ANO1, IP_3R, and G-protein coupled receptors (GPCR; type 2 bradykinin and protease-activated receptor-2 receptors) was shown to play a key role in driving Ca^{2+} signaling of small nociceptive neurons of dorsal root ganglia (Jin et al., 2013). Unlike PASMCs, Ca^{2+} entry through VGCC was unable to activate ANO1 in this system. In contrast, ANO1 was robustly stimulated by Ca^{2+} transients triggered by GPCR-mediated Ca^{2+} mobilization through IP_3R in portions of the endoplasmic reticulum making close contacts with caveolae within the PM indicating highly compartmentalized signaling. Evidence for a physical interaction between ANO1 and members of the canonical (TRPC) and vallinoid (TRPV) subfamilies of the transient receptor potential superfamily of cation channels was also reported in different cell types. Noxious stimuli such as capsaicin trigger repetitive action potential firing in sensory neurons through a specific interaction between localized Ca^{2+} entry through TRPV1 and ANO1-induced membrane depolarization (Takayama et al., 2015; Shah et al., 2020), a process amplified by ER Ca^{2+} release (Shah et al., 2020). Proximity ligation assays and superresolution microscopy established that ANO1, TRPV1, and type 1 IP_3R were closely associated with each other. In the apical membrane of choroid plexus epithelial cells, ANO1 physically and functionally interacts with TRPV4 to promote water efflux and maintain fluid drainage and cerebral spinal fluid movement in the brain. A similar scenario was proposed for saliva and tear production by exocrine acinar cells of the salivary and lacrimal glands (Derouiche et al., 2018). A physical association between ANO1 and TRPC6 was suggested to amplify the vasoconstriction produced by the specific TRPC6 agonist, Hyp9, in cerebral artery myocytes (Wang et al., 2016).

These examples highlight how specific ion channels are assembled in membrane nanodomains devised to produce optimal localized Ca^{2+} signaling that is unique to each cell's specific function. In the case of PASMCs, the molecular arrangement of ANO1, $Ca_V1.2$, and IP_3R appears to be geared toward supporting the generation and maintenance of intracellular Ca^{2+} waves initiated by Ca^{2+} release through IP_3R and propagated along the cell length by Ca^{2+}-induced Ca^{2+} release or CICR (Berridge et al., 2000; Berridge, 2009). Although our data suggest that only a few "triggering" sites appear to exist in each cell involving a few superclusters of ANO1-$Ca_V1.2$-IP_3R protein partners, a hypothesis supported by both our Ca^{2+} signaling and structural data, this hypothesis will require further testing with live-cell imaging experiments performed at higher temporal and spatial resolution. In an effort to partially address this question, PASMCs and tissues were exposed to MβCD to disrupt lipid rafts and caveolae, in particular (Rodal et al., 1999; Zidovetzki and Levitan, 2007; Patel et al., 2008). This protocol eradicated the superclusters and promoted an internalization of ANO1 and $Ca_V1.2$ that led to a similar decrease in force and Ca^{2+} signaling in response to 5-HT to that produced by blocking ANO1 or $Ca_V1.2$ pharmacologically or genetically. In contrast, the contraction mediated by high external K^+ was unaffected, which indicated that the MβCD treatment did not diminish the ability of the muscle to contract to a depolarizing stimulus leading to activation of $Ca_V1.2$, which is similar to that reported by Schach et al. (2008) in rat PA stimulated with phenylephrine. Moreover, membrane cholesterol depletion with MβCD enhanced ANO1 current in murine portal vein myocytes (Sones et al., 2010) and ANO1 expressed in HEK-293 cells (De Jesús-Pérez et al., 2018). Despite significant internalization of the two proteins following MβCD treatment, they are still present in sufficient amounts in the PM to support voltage-gated Ca^{2+} entry through $Ca_V1.2$ and ANO1 channel activity. Taken together, these observations suggest that the reduced EC coupling seen with MβCD was likely not linked to a reduction in PM ion channel activity but rather a destruction of their compartmentalized organization. However, we have to remain cautious when interpreting these results because membrane cholesterol depletion will have many more significant effects on other important signaling molecules such as the 5-HT receptors, G-proteins, and scaffolding proteins that may have coincidently led to the effects observed. Therefore, identifying the unique structural proteins involved in tethering ANO1-$Ca_V1.2$ in specific areas of the PM making close contact with IP_3R within superficial elements of the SR (e.g., junctophilin-2 [Pritchard et al., 2019], stromal interaction molecules 1 and 2 [STIM1/2; Sallinger et al., 2023]), and how they influence localized Ca^{2+} signaling will be key to support this hypothesis. It is fair to conclude from our results that the global working model of a simple uniformly distributed positive feedback loop between Ca^{2+} entry through $Ca_V1.2$- and ANO1-mediated membrane depolarization (Fig. 12 A) is too simplistic. It needs to be replaced by a compartmentalized model of agonist-mediated EC coupling that involves discrete membrane domains favoring amplification of Ca^{2+} signals originating primarily from IP_3R in the SR, likely with the aid of closely juxtaposed ANO1 and $Ca_V1.2$ (Fig. 12 B), whose specific function(s) will require further investigation.

Another major goal of the present study was to determine the true contribution of CaCC and ANO1 to the 5-HT-induced contraction using a genetic approach and use this strategy to validate the activity of one of the newer generations of ANO1 blockers. Two distinct smooth muscle-specific and inducible ANO1 knockout mice produced similar effects on the 5-HT-mediated contraction (~50–60% inhibition at higher 5-HT concentrations), which quantitatively mirrored those produced by

the ANO1 blocker $CaCC_{Inh}$-A01 in pulmonary arteries from wild-type mice. These results are similar to the reported inhibition by niflumic acid and nifedipine (both produced 35% inhibition) of the contraction to endothelin-1 of rat pulmonary arteries (Hyvelin et al., 1998). The concentration–response relationships to 5-HT in PA from wild-type mice and SMC-ANO1-KO-$^{\Delta Ex12}$ mice injected with vehicle (Control) were also quantitatively similar. In both transgenic mouse models used in the present study, induction of Cre recombinase for a minimum of 50 d after TMX injections led to a robust reduction in mRNA levels (>75%). The level of ANO1 knockdown detected by qRT-PCR in vascular smooth muscle from SMC-ANO1-KO-$^{\Delta Ex5/6}$ mice was similar to that reported for mouse collecting lymphatic vessels (Zawieja et al., 2019) and hindlimb arteries (Leo et al., 2021). Although we were unable to detect ANO1 protein by Western blot in total lysates from mouse pulmonary arteries, a band corresponding to the expected monomeric form of ANO1 (~110 kD) was successfully identified by Western blot after amplification through immunoprecipitation with the same ANO1 antibody used in Western blot assays from total protein lysates; this suggests that the protein is expressed in low abundance in this tissue under physiological conditions. The suppression of CaCC in PASMCs from SMC-ANO1-KO-$^{\Delta Ex12}$ mice confirmed that protein levels were potently downregulated following TMX induction of Cre recombinase. This is comparable to that reported in aortic smooth muscle cells from another TMX-inducible and smooth muscle-specific ANO1 knockout mouse model of which loxP sites flanked exon 21 (Heinze et al., 2014). Knockdown of ANO1 in this model lowered the blood pressure and attenuated the hypertensive effect of angiotensin II infusion, but not that produced by a high-salt diet. In our study, the tight correlation between the effects of $CaCC_{Inh}$-A01 in wild-type mice and genetic deletion of ANO1 in SMC-ANO1-KO mice, combined with a lack of effect of the compound in PA from the latter animals, support the notion that $CaCC_{Inh}$-A01 specifically targeted ANO1 and probably led to membrane hyperpolarization as was previously shown for the classical CaCC blocker niflumic acid in rat pulmonary arterial smooth muscle (Yuan, 1997). The conclusion is also supported by evidence showing that the compound exerted no influence on the contraction associated with high K^+-mediated membrane depolarization and Ca^{2+} entry through VGCC, which contrasted with the potent inhibitory effects of the $Ca_V1.2$ inhibitor nifedipine. It is important to mention that a recent study showed that $CaCC_{Inh}$-A01 inhibited Ca^{2+} release from internal stores in various cell types, presumably by blocking IP_3Rs (Genovese et al., 2023). Although such an effect was seen at a higher concentration than that used in this study, we cannot rule out that a component of the inhibition exerted by CaCCInh-A01 on the contraction and Ca^{2+} oscillations triggered by 5-HT might be attributable to the block of IP_3Rs, and more experiments are required to clarify this potential caveat. Our results are also at odds with those of Boedtkjer et al. (2015) who reported that $CaCC_{Inh}$-A01 concentration dependently inhibited the contraction of mouse mesenteric arteries to norepinephrine or U46619 in a manner that was independent of the Cl^- gradient across the membrane, therefore questioning the role of CaCC and ANO1 in agonist-mediated contractions. Similar conclusions were drawn by the same group for $T16A_{Inh}$-A01 and MONNA, two other newer generation CaCC inhibitors, but not supported by a more recent study in rat coronary artery smooth muscle (Askew Page et al., 2019). It is unclear if differences in experimental conditions or the use of different preparations were responsible for these apparent discrepancies, but additional experiments are necessary to reconcile these findings. Albeit smaller, a significant fraction of the contraction to 5-HT remained when either one of ANO1, $Ca_V1.2$, or SR Ca^{2+} release was inhibited. This contraction component may be attributed to one or more signaling pathways including receptor- (ROCE; Lin et al., 2004; Remillard and Yuan, 2006; Yamamura et al., 2011; Xia et al., 2014; Leblanc et al., 2015) or store-operated (SOCE; Lin et al., 2004; Remillard and Yuan, 2006; Ogawa et al., 2009; Forrest et al., 2010; Song et al., 2011; Yamamura et al., 2011; Liu et al., 2012; Ogawa et al., 2012; Leblanc et al., 2015; Wang et al., 2017) Ca^{2+} entry, or enhanced Ca^{2+} sensitivity of the contractile machinery due to engagement of the small RhoA/Rho kinases (Jernigan et al., 2004; Nagaoka et al., 2004; Broughton et al., 2008; Guilluy et al., 2009). This contraction component was not investigated in this study.

In conclusion, we provide novel functional and structural information unraveling a key role for ANO1 in determining a large component of the contraction of mouse PASMCs to the agonist serotonin. Although the detailed molecular mechanism still remains to be determined, our data support the hypothesis postulating that ANO1 works in concert with $Ca_V1.2$ in the PM to promote the initiation and maintenance of Ca^{2+} waves originating from Ca^{2+} mobilization from IP_3-dependent SR Ca^{2+} stores that cyclically spread along the main cell axis orientation to maintain force production. Consistent with this hypothesis was the demonstration of a close physical association of ANO1 with both $Ca_V1.2$ and IP_3R. This molecular microenvironment favors localized Ca^{2+} entry through $Ca_V1.2$ that stimulates membrane depolarization by neighboring ANO1, which may potentially serve an important role in repleting Ca^{2+} stores and lowering the threshold for stimulation of IP_3R by IP_3 and cytoplasmic Ca^{2+}. These results establish a mechanistic foundation that will assist in delineating in the future how increased ANO1 expression and function in PH (Forrest et al., 2012; Sun et al., 2012; Papp et al., 2019) leads to enhanced vasoconstriction and perhaps remodeling of smooth muscle cells in this disease.

Data availability

All study data are included in the article.

Acknowledgments

David A. Eisner served as editor.

The authors thank Lauren O'Kane for her technical assistance with the qRT-PCR experiments, and Dr. Yumei Feng-Earley, Gerald Bustos, and Dr. Blaine Harper for the management of all transgenic mouse lines through the Transgenic Animal Genotyping and Phenotyping Core of the Nevada Center of Biomedical Research Excellence (COBRE) for Molecular and Cellular Signal Transduction in the Cardiovascular System. We are also grateful for the technical assistance of Yung Kim with all

microscopy experiments, which were supported by the High Spatial and Temporal Imaging Core of the COBRE for Molecular and Cellular Signal Transduction in the Cardiovascular System.

This work was supported by National Institutes of Health grants to N. Leblanc (R01HL146054 and P20GM130459), S. Earley (R35HL155008, P20GM130459 and R01HL146054), J.H. Jaggar (HL155180, HL166411 and HL158846), and K.M. Sanders (R01DK120759), and by a British Heart Foundation grant to I.A. Greenwood (#FS/18/41/33762).

Authors contributions: N. Leblanc and I.A. Greenwood designed research; E.J. Akin, J. Aoun, C. Jimenez, K. Mayne, J. Baeck, M.D. Young, B. Sullivan, S.M. Ward, and N. Leblanc performed research; E.J. Akin, J. Aoun, and N. Leblanc wrote the manuscript; C. Jimenez, K.M. Sanders, S.M. Ward, S. Bulley, J.H. Jaggar, S. Earley, and I.A. Greenwood edited the manuscript.

Disclosures: The authors declare no competing interests exist.

Submitted: 24 June 2022
Revised: 1 August 2023
Accepted: 29 August 2023

References

Aickin, C.C., and A.F. Brading. 1982. Measurement of intracellular chloride in Guinea-pig vas deferens by ion analysis, 36chloride efflux and microelectrodes. *J. Physiol.* 326:139–154. https://doi.org/10.1113/jphysiol.1982.sp014182

Archer, S.L., E.K. Weir, and M.R. Wilkins. 2010. Basic science of pulmonary arterial hypertension for clinicians: New concepts and experimental therapies. *Circulation*. 121:2045–2066. https://doi.org/10.1161/CIRCULATIONAHA.108.847707

Askew Page, H.R., T. Dalsgaard, S.N. Baldwin, T.A. Jepps, O. Povstyan, S.P. Olesen, and I.A. Greenwood. 2019. TMEM16A is implicated in the regulation of coronary flow and is altered in hypertension. *Br. J. Pharmacol.* 176:1635–1648. https://doi.org/10.1111/bph.14598

Berg, J., H. Yang, and L.Y. Jan. 2012. Ca^{2+}-activated Cl^- channels at a glance. *J. Cell Sci.* 125:1367–1371. https://doi.org/10.1242/jcs.093260

Berridge, M.J. 2009. Inositol trisphosphate and calcium signalling mechanisms. *Biochim. Biophys. Acta*. 1793:933–940. https://doi.org/10.1016/j.bbamcr.2008.10.005

Berridge, M.J., P. Lipp, and M.D. Bootman. 2000. The versatility and universality of calcium signalling. *Nat. Rev. Mol. Cell Biol.* 1:11–21. https://doi.org/10.1038/35036035

Boedtkjer, D.M., S. Kim, A.B. Jensen, V.M. Matchkov, and K.E. Andersson. 2015. New selective inhibitors of calcium-activated chloride channels—T16A(inh) -A01, CaCC(inh) -A01 and MONNA—what do they inhibit? *Br. J. Pharmacol.* 172:4158–4172. https://doi.org/10.1111/bph.13201

Bradley, E., S. Fedigan, T. Webb, M.A. Hollywood, K.D. Thornbury, N.G. McHale, and G.P. Sergeant. 2014. Pharmacological characterization of TMEM16A currents. *Channels*. 8:308–320. https://doi.org/10.4161/chan.28065

Broughton, B.R., B.R. Walker, and T.C. Resta. 2008. Chronic hypoxia induces Rho kinase-dependent myogenic tone in small pulmonary arteries. *Am. J. Physiol. Lung Cell Mol. Physiol.* 294:L797–L806. https://doi.org/10.1152/ajplung.00253.2007

Bulley, S., and J.H. Jaggar. 2014. Cl^- channels in smooth muscle cells. *Pflugers Arch.* 466:861–872. https://doi.org/10.1007/s00424-013-1357-2

Chen, Q., M. Cannell, and C. van Breemen. 1992. The superficial buffer barrier in vascular smooth muscle. *Can. J. Physiol. Pharmacol.* 70:509–514. https://doi.org/10.1139/y92-066

Chipperfield, A.R., and A.A. Harper. 2000. Chloride in smooth muscle. *Prog. Biophys. Mol. Biol.* 74:175–221. https://doi.org/10.1016/S0079-6107(00)00024-9

Clark, J.H., N.P. Kinnear, S. Kalujnaia, G. Cramb, S. Fleischer, L.H. Jeyakumar, F. Wuytack, and A.M. Evans. 2010. Identification of functionally segregated sarcoplasmic reticulum calcium stores in pulmonary arterial smooth muscle. *J. Biol. Chem.* 285:13542–13549. https://doi.org/10.1074/jbc.M110.101485

Cortijo, J., M. Martí-Cabrera, E. Bernabeu, T. Domènech, J. Bou, A.G. Fernández, J. Beleta, J.M. Palacios, and E.J. Morcillo. 1997. Characterization of 5-HT receptors on human pulmonary artery and vein: Functional and binding studies. *Br. J. Pharmacol.* 122:1455–1463. https://doi.org/10.1038/sj.bjp.0701509

Dai, Y.P., S. Bongalon, W.J. Hatton, J.R. Hume, and I.A. Yamboliev. 2005. ClC-3 chloride channel is upregulated by hypertrophy and inflammation in rat and canine pulmonary artery. *Br. J. Pharmacol.* 145:5–14. https://doi.org/10.1038/sj.bjp.0706135

Darby, P.J., C.Y. Kwan, and E.E. Daniel. 2000. Caveolae from canine airway smooth muscle contain the necessary components for a role in Ca(2+) handling. *Am. J. Physiol. Lung Cell Mol. Physiol.* 279:L1226–L1235. https://doi.org/10.1152/ajplung.2000.279.6.L1226

De Jesús-Pérez, J.J., S. Cruz-Rangel, A.E. Espino-Saldaña, A. Martínez-Torres, Z. Qu, H.C. Hartzell, N.E. Corral-Fernandez, P. Pérez-Cornejo, and J. Arreola. 2018. Phosphatidylinositol 4,5-bisphosphate, cholesterol, and fatty acids modulate the calcium-activated chloride channel TMEM16A (ANO1). *Biochim. Biophys. Acta Mol. Cell Biol. Lipids*. 1863:299–312. https://doi.org/10.1016/j.bbalip.2017.12.009

De La Fuente, R., W. Namkung, A. Mills, and A.S. Verkman. 2008. Small-molecule screen identifies inhibitors of a human intestinal calcium-activated chloride channel. *Mol. Pharmacol.* 73:758–768. https://doi.org/10.1124/mol.107.043208

Derouiche, S., Y. Takayama, M. Murakami, and M. Tominaga. 2018. TRPV4 heats up ANO1-dependent exocrine gland fluid secretion. *FASEB J.* 32:1841–1854. https://doi.org/10.1096/fj.201700954R

Dixon, R.E., O. Vivas, K.I. Hannigan, and E.J. Dickson. 2017. Ground state depletion super-resolution imaging in mammalian cells. *J. Vis. Exp.* 56239. https://doi.org/10.3791/56239

Forrest, A.S., J.E. Angermann, R. Raghunathan, C. Lachendro, I.A. Greenwood, and N. Leblanc. 2010. Intricate interaction between store-operated calcium entry and calcium-activated chloride channels in pulmonary artery smooth muscle cells. *Adv. Exp. Med. Biol.* 661:31–55. https://doi.org/10.1007/978-1-60761-500-2_3

Forrest, A.S., T.C. Joyce, M.L. Huebner, R.J. Ayon, M. Wiwchar, J. Joyce, N. Freitas, A.J. Davis, L. Ye, D.D. Duan, et al. 2012. Increased TMEM16A-encoded calcium-activated chloride channel activity is associated with pulmonary hypertension. *Am. J. Physiol. Cell Physiol.* 303:C1229–C1243. https://doi.org/10.1152/ajpcell.00044.2012

Gafni, J., J.A. Munsch, T.H. Lam, M.C. Catlin, L.G. Costa, T.F. Molinski, and I.N. Pessah. 1997. Xestospongins: Potent membrane permeable blockers of the inositol 1,4,5-trisphosphate receptor. *Neuron*. 19:723–733. https://doi.org/10.1016/S0896-6273(00)80384-0

Gamper, N., V. Reznikov, Y. Yamada, J. Yang, and M.S. Shapiro. 2004. Phosphatidylinositol [correction] 4,5-bisphosphate signals underlie receptor-specific Gq/11-mediated modulation of N-type Ca^{2+} channels. *J. Neurosci.* 24:10980–10992. https://doi.org/10.1523/JNEUROSCI.3869-04.2004

Genovese, M., M. Buccirossi, D. Guidone, R. De Cegli, S. Sarnataro, D. di Bernardo, and L.J.V. Galietta. 2023. Analysis of inhibitors of the anoctamin-1 chloride channel (transmembrane member 16A, TMEM16A) reveals indirect mechanisms involving alterations in calcium signalling. *Br. J. Pharmacol.* 180:775–785. https://doi.org/10.1111/bph.15995

Guéguinou, M., A. Gambade, R. Félix, A. Chantôme, Y. Fourbon, P. Bougnoux, G. Weber, M. Potier-Cartereau, and C. Vandier. 2015. Lipid rafts, KCa/ClCa/Ca^{2+} channel complexes and EGFR signaling: Novel targets to reduce tumor development by lipids? *Biochim. Biophys. Acta*. 1848:2603–2620. https://doi.org/10.1016/j.bbamem.2014.10.036

Guibert, C., R. Marthan, and J.P. Savineau. 1996a. Angiotensin II-induced Ca(2+)-oscillations in vascular myocytes from the rat pulmonary artery. *Am. J. Physiol.* 270:L637–L642. https://doi.org/10.1152/ajplung.1996.270.4.L637

Guibert, C., P. Pacaud, G. Loirand, R. Marthan, and J.P. Savineau. 1996bb. Effect of extracellular ATP on cytosolic Ca^{2+} concentration in rat pulmonary artery myocytes. *Am. J. Physiol.* 271:L450–L458. https://doi.org/10.1152/ajplung.1996.271.3.L450

Guilluy, C., S. Eddahibi, C. Agard, C. Guignabert, M. Izikki, L. Tu, L. Savale, M. Humbert, E. Fadel, S. Adnot, et al. 2009. RhoA and Rho kinase activation in human pulmonary hypertension: Role of 5-HT signaling. *Am. J. Respir. Crit. Care Med.* 179:1151–1158. https://doi.org/10.1164/rccm.200805-691OC

György, I., and S. Györke. 1998. Regulation of the cardiac ryanodine receptor channel by luminal Ca^{2+} involves luminal Ca^{2+} sensing sites. *Biophys. J.* 75:2801–2810. https://doi.org/10.1016/S0006-3495(98)77723-9

Hamada, H., D.S. Damron, S.J. Hong, D.R. Van Wagoner, and P.A. Murray. 1997. Phenylephrine-induced Ca^{2+} oscillations in canine pulmonary artery smooth muscle cells. *Circ. Res.* 81:812–823. https://doi.org/10.1161/01.RES.81.5.812

Heinze, C., A. Seniuk, M.V. Sokolov, A.K. Huebner, A.E. Klementowicz, I.A. Szijártó, J. Schleifenbaum, H. Vitzthum, M. Gollasch, H. Ehmke, et al. 2014. Disruption of vascular Ca^{2+}-activated chloride currents lowers blood pressure. *J. Clin. Invest.* 124:675–686. https://doi.org/10.1172/JCI70025

Henriquez, M., M. Fonseca, and J.F. Perez-Zoghbi. 2018. Purinergic receptor stimulation induces calcium oscillations and smooth muscle contraction in small pulmonary veins. *J. Physiol.* 596:2491–2506. https://doi.org/10.1113/JP274731

Hirenallur-S, D.K., S.T. Haworth, J.T. Leming, J. Chang, G. Hernandez, J.B. Gordon, and N.J. Rusch. 2008. Upregulation of vascular calcium channels in neonatal piglets with hypoxia-induced pulmonary hypertension. *Am. J. Physiol. Lung Cell Mol. Physiol.* 295:L915–L924. https://doi.org/10.1152/ajplung.90286.2008

Huang, F., J.R. Rock, B.D. Harfe, T. Cheng, X. Huang, Y.N. Jan, and L.Y. Jan. 2009. Studies on expression and function of the TMEM16A calcium-activated chloride channel. *Proc. Natl. Acad. Sci. USA.* 106:21413–21418. https://doi.org/10.1073/pnas.0911935106

Huang, F., X. Wong, and L.Y. Jan. 2012. International union of basic and clinical pharmacology. LXXXV: Calcium-activated chloride channels. *Pharmacol. Rev.* 64:1–15. https://doi.org/10.1124/pr.111.005009

Hwang, S.J., P.J. Blair, F.C. Britton, K.E. O'Driscoll, G. Hennig, Y.R. Bayguinov, J.R. Rock, B.D. Harfe, K.M. Sanders, and S.M. Ward. 2009. Expression of anoctamin 1/TMEM16A by interstitial cells of Cajal is fundamental for slow wave activity in gastrointestinal muscles. *J. Physiol.* 587:4887–4904. https://doi.org/10.1113/jphysiol.2009.176198

Hyvelin, J.M., C. Guibert, R. Marthan, and J.P. Savineau. 1998. Cellular mechanisms and role of endothelin-1-induced calcium oscillations in pulmonary arterial myocytes. *Am. J. Physiol.* 275:L269–L282. https://doi.org/10.1152/ajplung.1998.275.2.L269

Jaggar, J.H., V.A. Porter, W.J. Lederer, and M.T. Nelson. 2000. Calcium sparks in smooth muscle. *Am. J. Physiol. Cell Physiol.* 278:C235–C256. https://doi.org/10.1152/ajpcell.2000.278.2.C235

Janssen, L.J., P.A. Betti, S.J. Netherton, and D.K. Walters. 1999. Superficial buffer barrier and preferentially directed release of Ca^{2+} in canine airway smooth muscle. *Am. J. Physiol.* 276:L744–L753. https://doi.org/10.1152/ajplung.1999.276.5.L744

Jernigan, N.L., B.R. Walker, and T.C. Resta. 2004. Chronic hypoxia augments protein kinase G-mediated Ca^{2+} desensitization in pulmonary vascular smooth muscle through inhibition of RhoA/Rho kinase signaling. *Am. J. Physiol. Lung Cell Mol. Physiol.* 287:L1220–L1229. https://doi.org/10.1152/ajplung.00196.2004

Jia, Z., and J. Chen. 2021. Specific PIP_2 binding promotes calcium activation of TMEM16A chloride channels. *Commun. Biol.* 4:259. https://doi.org/10.1038/s42003-021-01782-2

Jin, X., S. Shah, Y. Liu, H. Zhang, M. Lees, Z. Fu, J.D. Lippiat, D.J. Beech, A. Sivaprasadarao, S.A. Baldwin, et al. 2013. Activation of the Cl^- channel ANO1 by localized calcium signals in nociceptive sensory neurons requires coupling with the IP3 receptor. *Sci. Signal.* 6:ra73. https://doi.org/10.1126/scisignal.2004184

Jorgensen, A.O., A.C. Shen, W. Arnold, A.T. Leung, and K.P. Campbell. 1989. Subcellular distribution of the 1,4-dihydropyridine receptor in rabbit skeletal muscle in situ: An immunofluorescence and immunocolloidal gold-labeling study. *J. Cell Biol.* 109:135–147. https://doi.org/10.1083/jcb.109.1.135

Kitamura, K., and J. Yamazaki. 2001. Chloride channels and their functional roles in smooth muscle tone in the vasculature. *Jpn. J. Pharmacol.* 85:351–357. https://doi.org/10.1254/jjp.85.351

Ko, W., and B.C. Suh. 2021. Differential regulation of Ca^{2+}-activated Cl^- channel TMEM16A splice variants by membrane PI(4,5)P2. *Int. J. Mol. Sci.* 22:4088. https://doi.org/10.3390/ijms22084088

Large, W.A., and Q. Wang. 1996. Characteristics and physiological role of the Ca(2+)-activated Cl^- conductance in smooth muscle. *Am. J. Physiol.* 271:C435–C454. https://doi.org/10.1152/ajpcell.1996.271.2.C435

Le, S.C., Z. Jia, J. Chen, and H. Yang. 2019. Molecular basis of PIP_2-dependent regulation of the Ca^{2+}-activated chloride channel TMEM16A. *Nat. Commun.* 10:3769. https://doi.org/10.1038/s41467-019-11784-8

Le, S.C., P. Liang, A.J. Lowry, and H. Yang. 2021. Gating and regulatory mechanisms of TMEM16 ion channels and scramblases. *Front. Physiol.* 12:787773. https://doi.org/10.3389/fphys.2021.787773

Leblanc, N., A.S. Forrest, R.J. Ayon, M. Wiwchar, J.E. Angermann, H.A. Pritchard, C.A. Singer, M.L. Valencik, F. Britton, and I.A. Greenwood. 2015. Molecular and functional significance of Ca(2+)-activated Cl(−) channels in pulmonary arterial smooth muscle. *Pulm. Circ.* 5:244–268. https://doi.org/10.1086/680189

Leblanc, N., J. Ledoux, S. Saleh, A. Sanguinetti, J. Angermann, K. O'Driscoll, F. Britton, B.A. Perrino, and I.A. Greenwood. 2005. Regulation of calcium-activated chloride channels in smooth muscle cells: A complex picture is emerging. *Can. J. Physiol. Pharmacol.* 83:541–556. https://doi.org/10.1139/y05-040

Lee, K.P., J.P. Yuan, J.H. Hong, I. So, P.F. Worley, and S. Muallem. 2010. An endoplasmic reticulum/plasma membrane junction: STIM1/Orai1/TRPCs. *FEBS Lett.* 584:2022–2027. https://doi.org/10.1016/j.febslet.2009.11.078

Leo, M.D., D. Peixoto-Nieves, W. Yin, S. Raghavan, P. Muralidharan, A. Mata-Daboin, and J.H. Jaggar. 2021. TMEM16A channel upregulation in arterial smooth muscle cells produces vasoconstriction during diabetes. *Am. J. Physiol. Heart Circ. Physiol.* 320:H1089–H1101. https://doi.org/10.1152/ajpheart.00690.2020

Levet, F., E. Hosy, A. Kechkar, C. Butler, A. Beghin, D. Choquet, and J.B. Sibarita. 2015. SR-tesseler: A method to segment and quantify localization-based super-resolution microscopy data. *Nat. Methods.* 12:1065–1071. https://doi.org/10.1038/nmeth.3579

Liao, Y., C. Erxleben, J. Abramowitz, V. Flockerzi, M.X. Zhu, D.L. Armstrong, and L. Birnbaumer. 2008. Functional interactions among Orai1, TRPCs, and STIM1 suggest a STIM-regulated heteromeric Orai/TRPC model for SOCE/Icrac channels. *Proc. Natl. Acad. Sci. USA.* 105:2895–2900. https://doi.org/10.1073/pnas.0712288105

Liao, Y., N.W. Plummer, M.D. George, J. Abramowitz, M.X. Zhu, and L. Birnbaumer. 2009. A role for Orai in TRPC-mediated Ca^{2+} entry suggests that a TRPC:Orai complex may mediate store and receptor operated Ca^{2+} entry. *Proc. Natl. Acad. Sci. USA.* 106:3202–3206. https://doi.org/10.1073/pnas.0813346106

Lin, M.J., G.P. Leung, W.M. Zhang, X.R. Yang, K.P. Yip, C.M. Tse, and J.S. Sham. 2004. Chronic hypoxia-induced upregulation of store-operated and receptor-operated Ca^{2+} channels in pulmonary arterial smooth muscle cells: A novel mechanism of hypoxic pulmonary hypertension. *Circ. Res.* 95:496–505. https://doi.org/10.1161/01.RES.0000138952.16382.ad

Liu, J.Q., and R.J. Folz. 2004. Extracellular superoxide enhances 5-HT-induced murine pulmonary artery vasoconstriction. *Am. J. Physiol. Lung Cell Mol. Physiol.* 287:L111–L118. https://doi.org/10.1152/ajplung.00006.2004

Liu, X.R., M.F. Zhang, N. Yang, Q. Liu, R.X. Wang, Y.N. Cao, X.R. Yang, J.S. Sham, and M.J. Lin. 2012. Enhanced store-operated Ca^{2}+ entry and TRPC channel expression in pulmonary arteries of monocrotaline-induced pulmonary hypertensive rats. *Am. J. Physiol. Cell Physiol.* 302:C77–C87. https://doi.org/10.1152/ajpcell.00247.2011

Löhn, M., M. Fürstenau, V. Sagach, M. Elger, W. Schulze, F.C. Luft, H. Haller, and M. Gollasch. 2000. Ignition of calcium sparks in arterial and cardiac muscle through caveolae. *Circ. Res.* 87:1034–1039. https://doi.org/10.1161/01.RES.87.11.1034

Madl, J., J. Weghuber, R. Fritsch, I. Derler, M. Fahrner, I. Frischauf, B. Lackner, C. Romanin, and G.J. Schütz. 2010. Resting state Orai1 diffuses as homotetramer in the plasma membrane of live mammalian cells. *J. Biol. Chem.* 285:41135–41142. https://doi.org/10.1074/jbc.M110.177881

Mandegar, M., C.V. Remillard, and J.X. Yuan. 2002. Ion channels in pulmonary arterial hypertension. *Prog. Cardiovasc. Dis.* 45:81–114. https://doi.org/10.1053/pcad.2002.127491

Mandegar, M., and J.X. Yuan. 2002. Role of K+ channels in pulmonary hypertension. *Vascul. Pharmacol.* 38:25–33. https://doi.org/10.1016/S1537-1891(02)00123-4

McElroy, S.P., A.M. Gurney, and R.M. Drummond. 2008. Pharmacological profile of store-operated Ca(2+) entry in intrapulmonary artery smooth muscle cells. *Eur. J. Pharmacol.* 584:10–20. https://doi.org/10.1016/j.ejphar.2008.01.018

Monkawa, T., A. Miyawaki, T. Sugiyama, H. Yoneshima, M. Yamamoto-Hino, T. Furuichi, T. Saruta, M. Hasegawa, and K. Mikoshiba. 1995. Heterotetrameric complex formation of inositol 1,4,5-trisphosphate receptor subunits. *J. Biol. Chem.* 270:14700–14704. https://doi.org/10.1074/jbc.270.24.14700

Moudgil, R., E.D. Michelakis, and S.L. Archer. 2006. The role of k+ channels in determining pulmonary vascular tone, oxygen sensing, cell proliferation, and apoptosis: Implications in hypoxic pulmonary vasoconstriction and pulmonary arterial hypertension. *Microcirculation*. 13: 615–632. https://doi.org/10.1080/10739680600930222

Mu, Y.P., D.C. Lin, S.Y. Zheng, H.X. Jiao, J.S.K. Sham, and M.J. Lin. 2018. Transient receptor potential melastatin-8 activation induces relaxation of pulmonary artery by inhibition of store-operated calcium entry in normoxic and chronic hypoxic pulmonary hypertensive rats. *J. Pharmacol. Exp. Ther.* 365:544–555. https://doi.org/10.1124/jpet.117.247320

Nagaoka, T., Y. Morio, N. Casanova, N. Bauer, S. Gebb, I. McMurtry, and M. Oka. 2004. Rho/Rho kinase signaling mediates increased basal pulmonary vascular tone in chronically hypoxic rats. *Am. J. Physiol. Lung Cell Mol. Physiol.* 287:L665–L672. https://doi.org/10.1152/ajplung.00050.2003

Namkung, W., P.W. Phuan, and A.S. Verkman. 2011. TMEM16A inhibitors reveal TMEM16A as a minor component of calcium-activated chloride channel conductance in airway and intestinal epithelial cells. *J. Biol. Chem.* 286:2365–2374. https://doi.org/10.1074/jbc.M110.175109

Ng, L.C., S.M. Wilson, C.E. McAllister, and J.R. Hume. 2007. Role of InsP3 and ryanodine receptors in the activation of capacitative Ca^{2+} entry by store depletion or hypoxia in canine pulmonary arterial smooth muscle cells. *Br. J. Pharmacol.* 152:101–111. https://doi.org/10.1038/sj.bjp.0707357

Ogawa, A., A.L. Firth, K.A. Smith, M.V. Maliakal, and J.X. Yuan. 2012. PDGF enhances store-operated Ca^{2+} entry by upregulating STIM1/Orai1 via activation of Akt/mTOR in human pulmonary arterial smooth muscle cells. *Am. J. Physiol. Cell Physiol.* 302:C405–C411. https://doi.org/10.1152/ajpcell.00337.2011

Ogawa, A., A.L. Firth, W. Yao, M.M. Madani, K.M. Kerr, W.R. Auger, S.W. Jamieson, P.A. Thistlethwaite, and J.X. Yuan. 2009. Inhibition of mTOR attenuates store-operated Ca^{2+} entry in cells from endarterectomized tissues of patients with chronic thromboembolic pulmonary hypertension. *Am. J. Physiol. Lung Cell Mol. Physiol.* 297:L666–L676. https://doi.org/10.1152/ajplung.90548.2008

Oh, S.J., S.J. Hwang, J. Jung, K. Yu, J. Kim, J.Y. Choi, H.C. Hartzell, E.J. Roh, and C.J. Lee. 2013. MONNA, a potent and selective blocker for transmembrane protein with unknown function 16/anoctamin-1. *Mol. Pharmacol.* 84:726–735. https://doi.org/10.1124/mol.113.087502

Ovesný, M., P. Křížek, J. Borkovec, Z. Švindrych, and G.M. Hagen. 2014. ThunderSTORM: A comprehensive ImageJ plug-in for PALM and STORM data analysis and super-resolution imaging. *Bioinformatics*. 30: 2389–2390. https://doi.org/10.1093/bioinformatics/btu202

Papp, R., C. Nagaraj, D. Zabini, B.M. Nagy, M. Lengyel, D. Skofic Maurer, N. Sharma, B. Egemnazarov, G. Kovacs, G. Kwapiszewska, et al. 2019. Targeting TMEM16A to reverse vasoconstriction and remodelling in idiopathic pulmonary arterial hypertension. *Eur. Respir. J.* 53:1800965. https://doi.org/10.1183/13993003.00965-2018

Patel, H.H., F. Murray, and P.A. Insel. 2008. Caveolae as organizers of pharmacologically relevant signal transduction molecules. *Annu. Rev. Pharmacol. Toxicol.* 48:359–391. https://doi.org/10.1146/annurev.pharmtox.48.121506.124841

Patton, C. 2010. MaxChelator. https://somapp.ucdmc.ucdavis.edu/pharmacology/bers/maxchelator/downloads.htm (accessed May 1, 2019).

Perez, J.F., and M.J. Sanderson. 2005. The contraction of smooth muscle cells of intrapulmonary arterioles is determined by the frequency of Ca^{2+} oscillations induced by 5-HT and KCl. *J. Gen. Physiol.*. 125:555–567. https://doi.org/10.1085/jgp.200409217

Perez-Zoghbi, J.F., and M.J. Sanderson. 2007. Endothelin-induced contraction of bronchiole and pulmonary arteriole smooth muscle cells is regulated by intracellular Ca^{2+} oscillations and Ca^{2+} sensitization. *Am. J. Physiol. Lung Cell Mol. Physiol.* 293:L1000–L1011. https://doi.org/10.1152/ajplung.00184.2007

Pritchard, H.A., N. Leblanc, A.P. Albert, and I.A. Greenwood. 2014. Inhibitory role of phosphatidylinositol 4,5-bisphosphate on TMEM16A-encoded calcium-activated chloride channels in rat pulmonary artery. *Br. J. Pharmacol.* 171:4311–4321. https://doi.org/10.1111/bph.12778

Pritchard, H.A.T., C.S. Griffin, E. Yamasaki, P. Thakore, C. Lane, A.S. Greenstein, and S. Earley. 2019. Nanoscale coupling of junctophilin-2 and ryanodine receptors regulates vascular smooth muscle cell contractility. *Proc. Natl. Acad. Sci. USA*. 116:21874–21881. https://doi.org/10.1073/pnas.1911304116

Remillard, C.V., and J.X. Yuan. 2006. TRP channels, CCE, and the pulmonary vascular smooth muscle. *Microcirculation*. 13:671–692. https://doi.org/10.1080/10739680600930313

Rodal, S.K., G. Skretting, O. Garred, F. Vilhardt, B. van Deurs, and K. Sandvig. 1999. Extraction of cholesterol with methyl-beta-cyclodextrin perturbs formation of clathrin-coated endocytic vesicles. *Mol. Biol. Cell*. 10: 961–974. https://doi.org/10.1091/mbc.10.4.961

Rodat-Despoix, L., V. Aires, T. Ducret, R. Marthan, J.P. Savineau, E. Rousseau, and C. Guibert. 2009. Signalling pathways involved in the contractile response to 5-HT in the human pulmonary artery. *Eur. Respir. J.* 34: 1338–1347. https://doi.org/10.1183/09031936.00143808

Sallinger, M., H. Grabmayr, C. Humer, D. Bonhenry, C. Romanin, R. Schindl, and I. Derler. 2023. Activation mechanisms and structural dynamics of STIM proteins. *J. Physiol.* https://doi.org/10.1113/JP283828

Sanders, K.M., M.H. Zhu, F. Britton, S.D. Koh, and S.M. Ward. 2012. Anoctamins and gastrointestinal smooth muscle excitability. *Exp. Physiol.* 97: 200–206. https://doi.org/10.1113/expphysiol.2011.058248

Schach, C., A.L. Firth, M. Xu, C.V. Remillard, H.H. Patel, P.A. Insel, and J.X. Yuan. 2008. Regulation of pulmonary vasoconstriction by agonists and caveolae. *Exp. Lung Res.* 34:195–208. https://doi.org/10.1080/01902140801925471

Schneider, C.A., W.S. Rasband, and K.W. Eliceiri. 2012. NIH image to ImageJ: 25 years of image analysis. *Nat. Methods*. 9:671–675. https://doi.org/10.1038/nmeth.2089

Seidler, N.W., I. Jona, M. Vegh, and A. Martonosi. 1989. Cyclopiazonic acid is a specific inhibitor of the Ca^{2+}-ATPase of sarcoplasmic reticulum. *J. Biol. Chem.* 264:17816–17823. https://doi.org/10.1016/S0021-9258(19)84646-X

Shah, S., C.M. Carver, P. Mullen, S. Milne, V. Lukacs, M.S. Shapiro, and N. Gamper. 2020. Local Ca^{2+} signals couple activation of TRPV1 and ANO1 sensory ion channels. *Sci. Signal.* 13:eaaw7963. https://doi.org/10.1126/scisignal.aaw7963

Shaw, A.M., C. Brown, J. Irvine, D.C. Bunton, and A. MacDonald. 2000. Role of the 5-HT(2A)receptor and alpha(1)-adrenoceptor in the contractile response of rat pulmonary artery to 5-HT in the presence and absence of nitric oxide. *Pulm. Pharmacol. Ther.* 13:277–285. https://doi.org/10.1006/pupt.2000.0255

Smani, T., S. Iwabuchi, J. López-Barneo, and J. Ureña. 2001. Differential segmental activation of Ca^{2+} -dependent $Cl^-$and K+ channels in pulmonary arterial myocytes. *Cell Calcium*. 29:369–377. https://doi.org/10.1054/ceca.2001.0199

Sones, W.R., A.J. Davis, N. Leblanc, and I.A. Greenwood. 2010. Cholesterol depletion alters amplitude and pharmacology of vascular calcium-activated chloride channels. *Cardiovasc. Res.* 87:476–484. https://doi.org/10.1093/cvr/cvq057

Song, M.Y., A. Makino, and J.X. Yuan. 2011. STIM2 contributes to enhanced store-operated Ca entry in pulmonary artery smooth muscle cells from patients with idiopathic pulmonary arterial hypertension. *Pulm. Circ.* 1: 84–94. https://doi.org/10.4103/2045-8932.78106

Suh, B.C., D.I. Kim, B.H. Falkenburger, and B. Hille. 2012. Membrane-localized β-subunits alter the PIP2 regulation of high-voltage activated Ca^{2+} channels. *Proc. Natl. Acad. Sci. USA*. 109:3161–3166. https://doi.org/10.1073/pnas.1121434109

Sun, H., O. Paudel, and J.S.K. Sham. 2021. Increased intracellular Cl^- concentration in pulmonary arterial myocytes is associated with chronic hypoxic pulmonary hypertension. *Am. J. Physiol. Cell Physiol.* 321: C297–C307. https://doi.org/10.1152/ajpcell.00172.2021

Sun, H., Y. Xia, O. Paudel, X.R. Yang, and J.S. Sham. 2012. Chronic hypoxia-induced upregulation of Ca^{2+}-activated Cl^- channel in pulmonary arterial myocytes: A mechanism contributing to enhanced vasoreactivity. *J. Physiol.* 590:3507–3521. https://doi.org/10.1113/jphysiol.2012.232520

Ta, C.M., K.E. Acheson, N.J.G. Rorsman, R.C. Jongkind, and P. Tammaro. 2017. Contrasting effects of phosphatidylinositol 4,5-bisphosphate on cloned TMEM16A and TMEM16B channels. *Br. J. Pharmacol.* 174:2984–2999. https://doi.org/10.1111/bph.13913

Takayama, Y., D. Uta, H. Furue, and M. Tominaga. 2015. Pain-enhancing mechanism through interaction between TRPV1 and anoctamin 1 in sensory neurons. *Proc. Natl. Acad. Sci. USA*. 112:5213–5218. https://doi.org/10.1073/pnas.1421507112

Tembo, M., K.L. Wozniak, R.E. Bainbridge, and A.E. Carlson. 2019. Phosphatidylinositol 4,5-bisphosphate (PIP_2) and Ca^{2+} are both required to open the Cl^- channel TMEM16A. *J. Biol. Chem.* 294:12556–12564. https://doi.org/10.1074/jbc.RA118.007128

Thomas, C.M., and E.J. Smart. 2008. Caveolae structure and function. *J. Cell Mol. Med.* 12:796–809. https://doi.org/10.1111/j.1582-4934.2008.00295.x

Uma, S., M. Tuncer, and S.O. Kayaalp. 1987. The subtype of serotonin (5-HT) receptors in the rat pulmonary artery. *Arch. Int. Pharmacodyn. Ther.* 288: 248–255.

van Breemen, C., Q. Chen, and I. Laher. 1995. Superficial buffer barrier function of smooth muscle sarcoplasmic reticulum. *Trends Pharmacol. Sci.* 16:98–105. https://doi.org/10.1016/S0165-6147(00)88990-7

Wang, J., C. Xu, Q. Zheng, K. Yang, N. Lai, T. Wang, H. Tang, and W. Lu. 2017. Orai1, 2, 3 and STIM1 promote store-operated calcium entry in pulmonary arterial smooth muscle cells. *Cell Death Discov.* 3:17074. https://doi.org/10.1038/cddiscovery.2017.74

Wang, Q., M.D. Leo, D. Narayanan, K.P. Kuruvilla, and J.H. Jaggar. 2016. Local coupling of TRPC6 to ANO1/TMEM16A channels in smooth muscle cells amplifies vasoconstriction in cerebral arteries. *Am. J. Physiol. Cell Physiol.* 310:C1001–C1009. https://doi.org/10.1152/ajpcell.00092.2016

Woll, K.A., and F. Van Petegem. 2022. Calcium-release channels: Structure and function of IP_3 receptors and ryanodine receptors. *Physiol. Rev.* 102: 209–268. https://doi.org/10.1152/physrev.00033.2020

Wu, L., C.S. Bauer, X.G. Zhen, C. Xie, and J. Yang. 2002. Dual regulation of voltage-gated calcium channels by PtdIns(4,5)P2. *Nature.* 419:947–952. https://doi.org/10.1038/nature01118

Xia, Y., X.R. Yang, Z. Fu, O. Paudel, J. Abramowitz, L. Birnbaumer, and J.S. Sham. 2014. Classical transient receptor potential 1 and 6 contribute to hypoxic pulmonary hypertension through differential regulation of pulmonary vascular functions. *Hypertension.* 63:173–180. https://doi.org/10.1161/HYPERTENSIONAHA.113.01902

Yamamura, A., Q. Guo, H. Yamamura, A.M. Zimnicka, N.M. Pohl, K.A. Smith, R.A. Fernandez, A. Zeifman, A. Makino, H. Dong, and J.X. Yuan. 2012. Enhanced Ca(2+)-sensing receptor function in idiopathic pulmonary arterial hypertension. *Circ. Res.* 111:469–481. https://doi.org/10.1161/CIRCRESAHA.112.266361

Yamamura, A., H. Yamamura, A. Zeifman, and J.X. Yuan. 2011. Activity of Ca -activated Cl channels contributes to regulating receptor- and store-operated Ca entry in human pulmonary artery smooth muscle cells. *Pulm. Circ.* 1:269–279. https://doi.org/10.4103/2045-8932.83447

Yang, X.R., A.H. Lin, J.M. Hughes, N.A. Flavahan, Y.N. Cao, W. Liedtke, and J.S. Sham. 2012. Upregulation of osmo-mechanosensitive TRPV4 channel facilitates chronic hypoxia-induced myogenic tone and pulmonary hypertension. *Am. J. Physiol. Lung Cell Mol. Physiol.* 302: L555–L568. https://doi.org/10.1152/ajplung.00005.2011

Yang, X.R., M.J. Lin, K.P. Yip, L.H. Jeyakumar, S. Fleischer, G.P. Leung, and J.S. Sham. 2005. Multiple ryanodine receptor subtypes and heterogeneous ryanodine receptor-gated Ca^{2+} stores in pulmonary arterial smooth muscle cells. *Am. J. Physiol. Lung Cell Mol. Physiol.* 289: L338–L348. https://doi.org/10.1152/ajplung.00328.2004

Yu, Y., I. Fantozzi, C.V. Remillard, J.W. Landsberg, N. Kunichika, O. Platoshyn, D.D. Tigno, P.A. Thistlethwaite, L.J. Rubin, and J.X. Yuan. 2004. Enhanced expression of transient receptor potential channels in idiopathic pulmonary arterial hypertension. *Proc. Natl. Acad. Sci. USA.* 101: 13861–13866. https://doi.org/10.1073/pnas.0405908101

Yuan, J.X., A.M. Aldinger, M. Juhaszova, J. Wang, J.V. Conte Jr., S.P. Gaine, J.B. Orens, and L.J. Rubin. 1998a. Dysfunctional voltage-gated K+ channels in pulmonary artery smooth muscle cells of patients with primary pulmonary hypertension. *Circulation.* 98:1400–1406. https://doi.org/10.1161/01.CIR.98.14.1400

Yuan, X.J. 1997. Role of calcium-activated chloride current in regulating pulmonary vasomotor tone. *Am. J. Physiol.* 272:L959–L968. https://doi.org/10.1152/ajplung.1997.272.5.L959

Yuan, X.J., J. Wang, M. Juhaszova, S.P. Gaine, and L.J. Rubin. 1998b. Attenuated K+ channel gene transcription in primary pulmonary hypertension. *Lancet.* 351:726–727. https://doi.org/10.1016/S0140-6736(05)78495-6

Zawieja, S.D., J.A. Castorena, P. Gui, M. Li, S.A. Bulley, J.H. Jaggar, J.R. Rock, and M.J. Davis. 2019. Ano1 mediates pressure-sensitive contraction frequency changes in mouse lymphatic collecting vessels. *J. Gen. Physiol.* 151:532–554. https://doi.org/10.1085/jgp.201812294

Zhang, S., H.H. Patel, F. Murray, C.V. Remillard, C. Schach, P.A. Thistlethwaite, P.A. Insel, and J.X. Yuan. 2007. Pulmonary artery smooth muscle cells from normal subjects and IPAH patients show divergent cAMP-mediated effects on TRPC expression and capacitative Ca^{2+} entry. *Am. J. Physiol. Lung Cell Mol. Physiol.* 292:L1202–L1210. https://doi.org/10.1152/ajplung.00214.2006

Zheng, Y.M., Q.S. Wang, R. Rathore, W.H. Zhang, J.E. Mazurkiewicz, V. Sorrentino, H.A. Singer, M.I. Kotlikoff, and Y.X. Wang. 2005. Type-3 ryanodine receptors mediate hypoxia-but not neurotransmitter-induced calcium release and contraction in pulmonary artery smooth muscle cells. *J. Gen. Physiol.* 125:427–440. https://doi.org/10.1085/jgp.200409232

Zhu, M.H., T.W. Kim, S. Ro, W. Yan, S.M. Ward, S.D. Koh, and K.M. Sanders. 2009. A Ca(2+)-activated Cl(–) conductance in interstitial cells of Cajal linked to slow wave currents and pacemaker activity. *J. Physiol.* 587: 4905–4918. https://doi.org/10.1113/jphysiol.2009.176206

Zidovetzki, R., and I. Levitan. 2007. Use of cyclodextrins to manipulate plasma membrane cholesterol content: Evidence, misconceptions and control strategies. *Biochim. Biophys. Acta.* 1768:1311–1324. https://doi.org/10.1016/j.bbamem.2007.03.026

Supplemental material

Video 1. **Video depicting lack of spontaneous activity in an intact PA from a conditional SMC-GCaMP3 mouse exposed to normal external solution.** Stacked images (512 × 512 pixels) from a subset (150 frames) of the original video (1,000 images) were recorded at a frame rate of 32 F/s. All images were background subtracted, smoothened, and pseudo-colored to the Red Hot LUT table in ImageJ.

Video 2. **Video showing that a 5-min exposure to 1 µM 5-HT triggered asynchronous Ca^{2+} oscillations in the same PA from a conditional SMC-GCaMP3 mouse as shown in** Video 1**.** Stacked images (512 × 512 pixels) from a subset (150 frames) of the original movie (1,000 images) were recorded at a frame rate of 32 F/s. All images were background subtracted, smoothened, and pseudo-colored to the Red Hot LUT table in ImageJ.

Video 3. **Surface Plot video illustrating the initiation and propagation of Ca^{2+} waves in a single PASMC from an intact pulmonary artery from a conditional SMC-GCaMP3 mouse.** Stacked images (512 × 512 pixels) from the original movie were first cropped to images of 115 × 115 pixels in size. All images were background subtracted, smoothened, and pseudo-colored to the 5 Ramps LUT table in ImageJ. The resulting 2-D video was then processed to a 3-D video using the Surface Plot feature of ImageJ. The movie was slowed down four times to 8 F/s from the original 32 F/s. The movie contains a sequence of 200 images from the original 1,000 images.

Video 4. **Video showing that a 10-min exposure to 10 µM $CaCC_{Inh}$-A01 in the presence of 5-HT had a profound inhibitory effect on Ca^{2+} oscillations in the same pulmonary artery from a conditional SMC-GCaMP3 mouse as shown in** Videos 1 and 2**.** Stacked images (512 × 512 pixels) from a subset (150 frames) of the original video (1,000 images) were recorded at a frame rate of 32 F/s. All images were background subtracted, smoothened, and pseudo-colored to the Red Hot LUT table in ImageJ.